博士論文

Thermodynamic and Structural Analyses of a Layered Solid Acid Absorbed Ammonia

（アンモニアを吸蔵した層状固体酸の熱力学的解析及び構造解析）

山　口　　匡　訓

広島大学大学院先端物質科学研究科

2021 年 3 月

目次

1. 主論文

2. 公表論文

3. 参考論文

(2) Investigation on standard entropy change of metal hydrides and work function of metals
Yoshitsugu Kojima and Masakuni Yamaguchi
International Journal of Hydrogen Energy, **46(2)**, 2306-2311 (2021).

(3) Thermodynamic analysis of ammonia storage materials
Yoshitsugu Kojima and Masakuni Yamaguchi
International Journal of Hydrogen Energy, **46(21)**, 11756-11760 (2021).

主論文

Abstract

Ammonia is useful both as a hydrogen carrier and a fuel. Although, ammonia has the same level of toxicity as other hydrogen carrier materials. Therefore, it is necessary to remove ammonia immediately from space in the case of leakage. In this thesis, we studied the following topics; (i) ammonia ad/absorption characteristics of insoluble proton-based solid acids, and (ii) thermodynamic and structural analyses of zirconium phosphate absorbed ammonia.

(i) Ammonia ad/absorption characteristics of insoluble proton-based solid acids

We proposed a new ammonia removal system combining water and an insoluble proton-based solid acid and measured the ammonia ad/absorption properties of various insoluble proton based solid acids in ammonia water. Zirconium phosphate (ZrP, $Zr(HPO_4)_2 \cdot H_2O$, a layered structure) has large ammonia storage capacity 10.2 wt% among proton-based solid acids and low ammonia vapor concentration below 2 ppm. The new system combining water and ZrP can greatly reduce the residual ammonia concentration in the space from 1000 ppm to 0.5 ppm as compared to water. Since ZrP is insoluble in water after the ammonia absorption, it can be separated easily from water solution.

(ii) Thermodynamic and structural analyses of zirconium phosphate absorbed ammonia

Ammonia absorption properties of ZrP was investigated by ammonia concentration composition isotherm (CCI) measurements. Two thermodynamic equilibrium plateau concentrations of ZrP were found during the ammonia absorption. The standard heat of formation ΔH^0 and the standard entropy change ΔS^0 were estimated by van't Hoff plot. These ΔH^0 and ΔS^0 values of ZrP absorbed ammonia (1-2 mol(NH_3)mol^{-1}(ZrP)) are similar to whose of ammonia absorption reactions of ammonium bisulfate (NH_4HSO_4). Moreover, a two-step structural phase transition was found during ammonia absorption in ZrP. The structural phase transition mainly by the expansion of interlayer distance was confirmed by the X-ray diffraction (XRD). The local structures of ZrP absorbed ammonia from 0 to 1 mol(NH_3)mol^{-1}(ZrP) and that from 1 to 2 mol(NH_3)mol^{-1}(ZrP) were different by ^{31}P magic angle spinning nuclear magnetic resonance (^{31}P MAS NMR) and Fourier transform infrared (FTIR) spectroscopy. It was found that ammonia attaches to the phosphate groups ($Zr(HPO_4)_2 \cdot H_2O$) to form ammonium ion, and ZrP absorbed ammonia (2 mol(NH_3)mol^{-1}(ZrP)) has two hydrogen bonds of one ammonia ion in two places connecting the layers to one phosphate group in each layer. We believe that this condition caused ZrP to absorb a large amount of ammonia even at low concentrations.

This phenomenon is thought to originate from the layered structure. Therefore, a layered structure is the key to an ammonia removal.

Contents

1.Introduction ・・・

List of Symbols

T: absolute temperature

G: Gibbs free energy

Δ: symbol for "an increment of "

H: enthalpy

S: entropy

R: gas constant (8.3144626 J K^{-1} mol^{-1})

P: pressure

P_0: standard pressure (0.1 MPa)

ΔH^0: standard heat of formation from gas (kJ mol^{-1})

ΔS^0: standard entropy change from gas (J $mol^{-1}K^{-1}$)

K: Henry's law constant

f: degrees of freedom

c: number of components

p: number of phases

c_m: mole fraction of ammonia

ΔH_s^0: standard heat of dissolution

ΔS_s^0: standard entropy change by dissolution

ΔH_w^0: standard heat of formation from water

ΔS_w^0: standard entropy change from water

η: hydrogen conversion efficiency

ΔH_h^0: standard heat of formation of water (higher heating value)

K_b: base dissociation constant

C_{st}: ammonia storage capacity

pH: potential of hydrogen

L: volme of ammonia water

M_{NH3}: molar mass of NH_3

M_{NH4+}: molar mass of NH_4^+

M_N: molar mass of N

C_0: standard state ammonia concentration

n: integer

θ: angle

d: interplanar spacing

λ: wavelength of X-ray

ΔE: energy difference

h: Planck constant

γ: gyromagnetic ratio

ν: resonance frequency

σ: shielding constant

B_0: magnetic field

δ: chemical shift

ν_{fv}: frequency of vibration

k: spring constant

m: mass

M: reduced mass

W_a: ammonia storage capacity

P_{ec}: proton exchange capacity

C_{eq}: ammonia equilibrium concentration

M_{H2O}: molar mass of H_2O

ρ_{H2O}: density of H_2O

1. Introduction

1.1 Energy transition

Fossil fuels

Fossil fuels are mainly coal, natural gas and petroleum. Since the energy of coal for steam engines during the industrial revolution of the 19th century, fossil fuels consumption is on the rise [1,2]. About 85% of the energy consumption is based on the fossil fuels with respect to global energy consumption in 2019 [3]. However, the emission of carbon dioxide from the energy usage of fossil fuels are driving global warming and air pollution. The problem of global warming caused by carbon dioxide has become a major issue since the first world conference on global warming (the Philaha Conference) held in 1985 in Villach, Austria. In 1988, the Intergovernmental Panel on Climate Change (IPCC) was established by the United Nations Environment Programme (UNEP) and the World Meteorological Organization (WMO) as an intergovernmental forum for the scientific aspects of global warming [4]. To prevent various adverse effects of global warming, the United Nations Framework Convention on Climate Change (UNFCCC) was entered into force in 1994 [4].

In 2015, the Paris Agreement proposed on efforts to reduce greenhouse gas (GHG: carbon dioxide, methane and so on) that cause global warming at the 21th session of the Conference of the Parties to the United Nations Framework Convention on Climate Change (COP21) [5]. The goal is to keep the average global temperature rise below 2 ℃ compared to pre-industrial levels (2 ℃ target), as well as efforts to limit it to 1.5 ℃

(1.5°C target). It also states that net anthropogenic GHG emissions should be reduced to zero in the second half of the 21st century [1-5]. China is now aiming toward a decarbonized society by 2060. EU is also aiming for this by 2050. Recently, the aim of Japan is to reduce GHG emission to 26% by 2030 and 80% by 2050. Moreover, Japanese Prime Minister Suga announced that Japan should reduce greenhouse gas emissions to virtually zero by 2050 as a pillar of its growth strategy in the G20 Riyadh Summit [6].

The transition to a decarbonized economy in the world is essential. Bloomberg NEF (Bloomberg New Energy Finance Ltd.) expects the energy consumption in 2020 to drop especially the consumption of fossil fuels, due to the increase in remote work and other factors for the corona pandemic. It is based on the assumption that competitive renewable energy sources (solar, wind, and hydro etc.) will lead to massive capital deployment, widespread adoption of electric vehicles (EVs), and increased energy efficiency in the industry as a whole [7].

Renewable energy

The renewable energy is also called alternative energy and that always present in nature such as solar, wind, hydro, tidal, geothermal, and biomass [8,9]. Its three characteristics are that it does not deplete, it is ubiquitous, it does not emit (or does not increase) carbon dioxide.

Energy demand is mainly classified into three categories; heat, transportation, and electricity, which account for 51, 32, and 17%, respectively in the world 2017 [10]. Then, the supply ratio from renewable energy sources is 10.6% (heat:10.1%, transportation:3.3%, and

electricity:26.4%) in 2017 [10]. Towards a decarbonized society, the use of renewable energy will have to be increased. However, the renewable energy is localized, and it has fluctuating output with weather and time. Thus, renewable energy should be converted to secondary energy such as electricity or hydrogen for responding the demand. Various energy storage technologies are required for efficient utilization of renewable energy in the world [11-13].

Energy storage technologies

Energy storage technology is a significant issue because it can level out the temporal and spatial variations of renewable energy. These technologies can be categorized into two main types: stationary storage and energy carrier [11-15].

Stationary storage technologies are categorized into a mechanical energy storage (MES) system, an electrical energy storage (EES) system, a thermal energy storage (TES) system and electrochemical energy storage (ECES).

The MES systems convert into a potential or a kinetic energy to use gravity or motion. The potential energy storage includes a pumped hydro storage (PHS) and a compressed air energy storage (CAES). The kinetic energy storage includes a flywheel energy storage (FES) system. The MES systems are suitable for massive energy storage and have a longer life than other technologies. Although, there are restrictions on locations and special techniques are required to operate.

The EES systems are categorized into electrostatic energy storage

system including electric double layer capacitor (EDLC), and magnetic/current storage system including magnetic energy storage (SMES). These systems have high energy conversion efficiency and high response. However, these systems have low energy density, relatively.

The TES systems mainly use changes in the internal energy of materials to store energy in thermal form such as sensible heat or latent heat. These systems are suitable for the storage of solar heat and waste heat. Although, thermal energy storage materials have a fixed limit to their energy conversion efficiency by Carnot's theorem.

The ECES systems store electricity under a chemical form such as secondary batteries and hydrogen-based energy storage systems. The secondary batteries are mainly lithium-ion batteries (LIB), nickel-metal hydride (Ni-MH) batteries, sodium-sulfur (NAS) batteries, redox-flow batteries (RFB), and lead-acid batteries. The hydrogen-based system is a fuel cell with high-pressure H_2 gas tank. These systems have high energy density. However, these systems are generally difficult to transmit power at maximum output over the four hours or more required as long-term storage.

The storage technology with energy carriers is a technology that converts energy into a transportable energy medium such as hydrogen. This technology uses chemical bonds within molecules to store chemical energy. Although its energy conversion efficiency is low, energy carrier is transportable and is expected to be used as an alternative fuel to fossil fuels. When considering their use as an alternative to fossil fuels, liquid form is considered to be preferred energy carriers from the viewpoint of

transportation, storage, and utilization. Recently, many researchers focus on energy carriers such as liquid hydrogen (H_2), methylcyclohexane (C_7H_{14}) and ammonia (NH_3) which are suitable as substances that can store large amounts of energy for longer. These are also called hydrogen storage materials.

Figure 1.1 shows gravimetric and volumetric energy densities of the above energy storage technologies. Hydrogen storage materials have large energy densities above 1000 $Whkg^{-1}$ and 1000 WhL^{-1} among them.

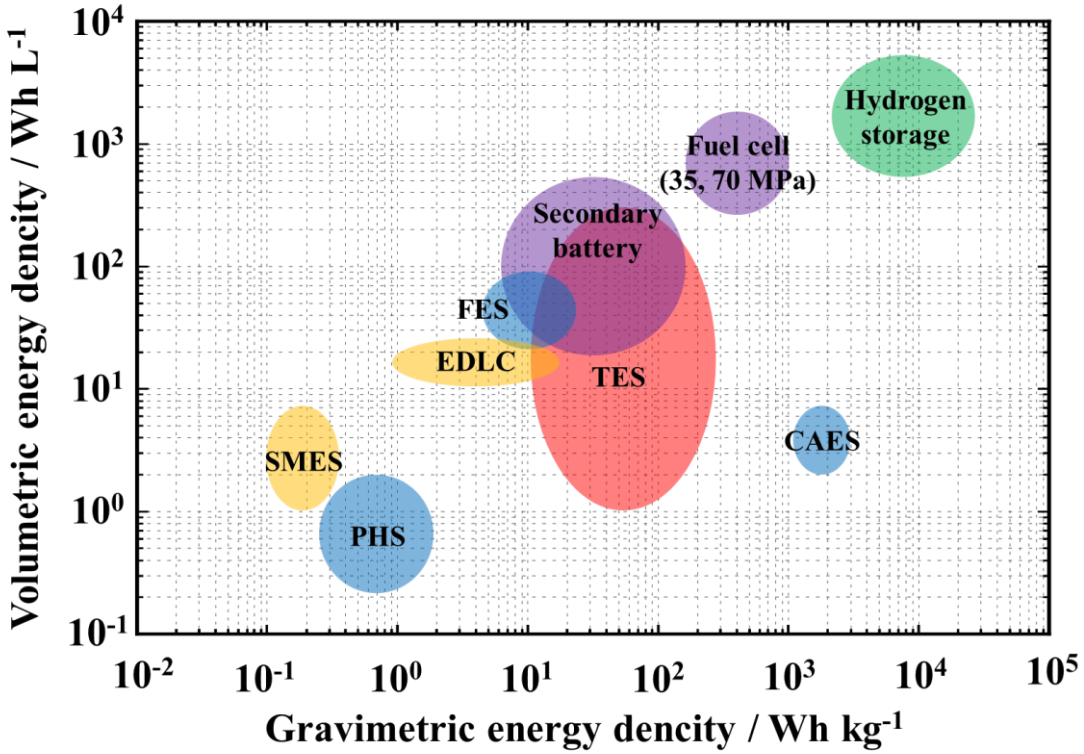

Figure 1.1 The relation between gravimetric and volumetric energy density of energy storage techniques. Blue circle: mechanical energy storage (MES), yellow circle: electrical energy storage (EES), red circle: thermal energy storage (TES), purple circle: electrochemical energy storage (ECES), green circle: hydrogen storage [11-15].

1.2 Thermodynamics

For utilization of hydrogen storage materials, it is necessary to absorb and desorb hydrogen from them by controlling temperature or pressure. Therefore, it is important to understand the thermodynamic conditions for the hydrogen absorption and desorption. In this chapter, the thermodynamics for the metal and hydrogen system are explained as representative one [16].

The equation for hydrogen absorption by a metal (M) to form a metal hydride is the following reaction equation.

$$M + a\,H_2 \rightarrow MH_{2a} \qquad \text{(Equation 1.2.1)}$$

The change in standard Gibbs free energy ΔG^0 is written by follows,

$$\Delta G^0 = \Delta H^0 - T\Delta S^0 \qquad \text{(Equation 1.2.2)}$$

$$\Delta G = \Delta G^0 - RT\ln(P/P_o) \qquad \text{(Equation 1.2.3)}$$

where T is the reaction temperature (K), ΔH^0 is the standard enthalpy change (kJ mol^{-1}), ΔS^0 is the standard entropy change (J mol^{-1} K^{-1}), ΔG is the change in Gibbs free energy (kJ mol^{-1}), P is the pressure of hydrogen (kPa), and P_0 is the standard pressure (101.325 kPa).

In $\Delta G = 0$, the chemical reaction is thermodynamic equilibrium state. Therefore, the hydrogen absorption and desorption of the hydrogen storage material occur to the same rate. In $\Delta G < 0$, reactions proceed spontaneously. In $\Delta G > 0$, reactions do not proceed spontaneously. When ΔH^0 is negative value of the above equation, the reaction exothermically proceeds. When ΔH^0 is positive value, the increase in temperature or decrease in H_2

pressure are required to satisfy $\Delta G < 0$. Therefore, temperature and pressure control the reaction.

The van't Hoff equation is obtained by using the above-mentioned P and standard thermodynamic parameters (ΔH^0, ΔS^0) as follows,

$$\ln\left(\frac{P}{P_0}\right) = \frac{\Delta H^0}{RT} - \frac{\Delta S^0}{R} \qquad \text{(Equation 1.2.4)}$$

ΔH^0 and ΔS^0 are estimated from the slope and intercept of the straight line plotting the logarithm of P/P_0 ($\ln P/P_0$) and reciprocal temperature ($1/T$) called the van't Hoff plot. The equation also shows that pressure depends on temperature.

The phase diagrams of hydrogen storage materials are constructed from the H_2 pressure composition isotherm (PCI) measurements as shown Figure 1.2(i), which is obtained by the isothermal measurement of the equilibrium H_2 content in the materials as a function of the H_2 pressure.

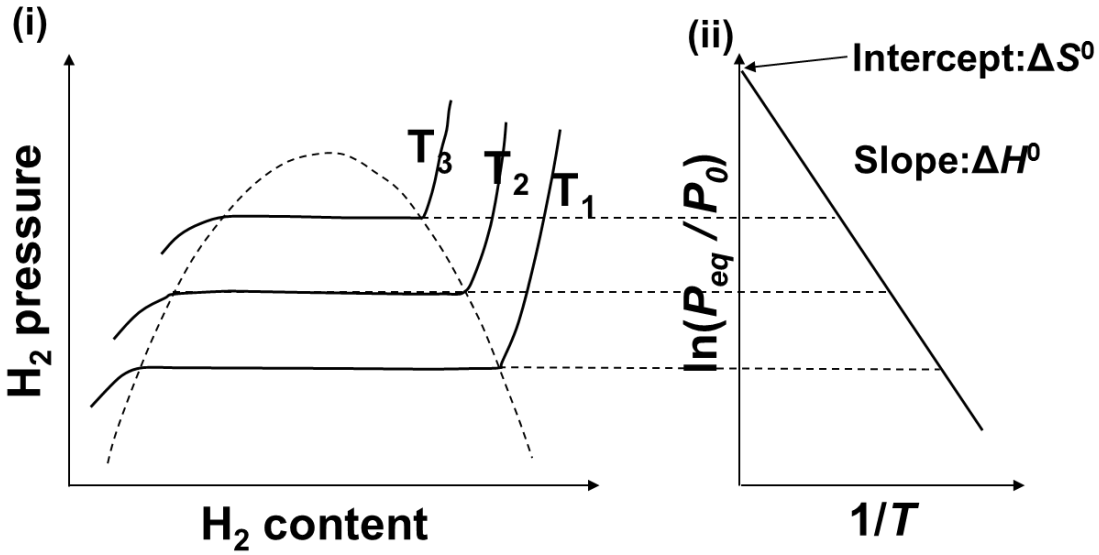

Figure 1.2 (i)Schematic view of pressure composition isotherms (PCIs), (ii) van't Hoff plot

In the plateau region, pressure does not change, and only hydrogen composition change. H_2 is successively absorbed in the material and the crystal structure of host material is generally changed by forming the bond between hydrogen and the material. At the ideal equilibrium condition, the H_2 pressure is constant even though H_2 is continuously absorbed in the material. This phenomenon is described by following Gibbs phase rule,

$$f = c - p + 2 \qquad \text{(Equation 1.2.5)}$$

where f is the degrees of freedom, c and p are the number of components and phases in the system. From equation 1.2.5, in the idealized equilibrium state, c is 2 (H_2 and M) and p is 3 (gas phase (H_2) and two solid phases (M and MH_{2a})), so f is 1. Therefore, in the PCI experiments, the pressure at equilibrium is constant because the temperature is fixed.

1.3 Hydrogen storage materials

Hydrogen storage materials store hydrogen atom or molecular hydrogen. The hydrogen atom has three states in its electronic states, protide (hydride) H^-, protium H^0 and proton H^+ based on the electronegativity difference from adjacent atoms. Hydrogen forms bonding to elements with lower electronegativity such as boron and aluminum as negative charged state (B-H, Al-H). Hydrogen forms bonding to elements with higher electronegativity such as carbon and nitrogen as positive charged state (C-H, N-H). In the hydride of transition metals such as Ti, V, Zr, Pd, La and Ce, hydrogen is protium [17].

Since solid hydrogen storage materials have gaps, the packing ratio should be taken into account when calculating the volumetric H_2 density. Assuming that the materials are ideal spherical shape, the theoretical packing ratio in both face-centered cubic (fcc) and hexagonal closed packed (hcp) lattices is 74% as shown in Figure 1.3.1. The ratio drops down to

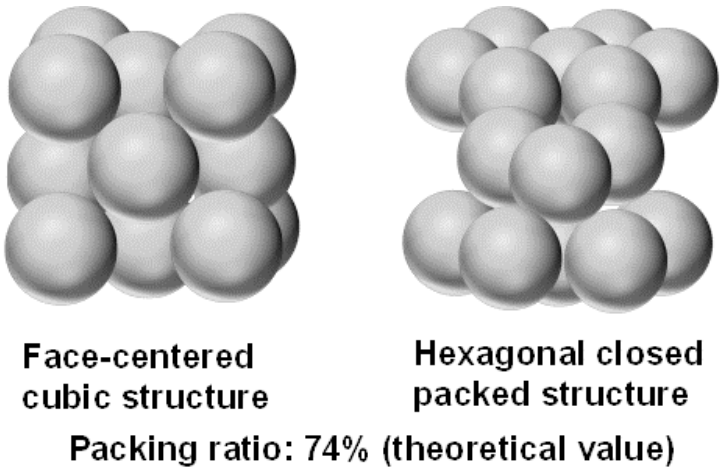

Figure 1.3.1 Face-centered cubic (fcc) structure and hexagonal closed packed (hcp) structure of solid materials

40-50% for real situation [18].

Hydrogen densities of hydrogen storage materials

Figure 1.3.2 shows calculated theoretical H_2 densities of hydrides and experimental values of hydrogen storage alloys, inorganic chemical hydrides and carbon materials. The value for liquid H_2 at 20 K (7.08 kg(H_2) / 100L [19]) are also shown in the figure for comparison.

Ammonia (NH_3) is easily liquefied (1 MPa and 298 K) and has a volumetric H_2 density 1.5 times higher than liquid H_2. The value is ten times compared with hydrogen storage alloys.

NH_3 has advantages as a hydrogen carrier, which transport large amount of hydrogen, and an energy carrier, which is a substance that can be

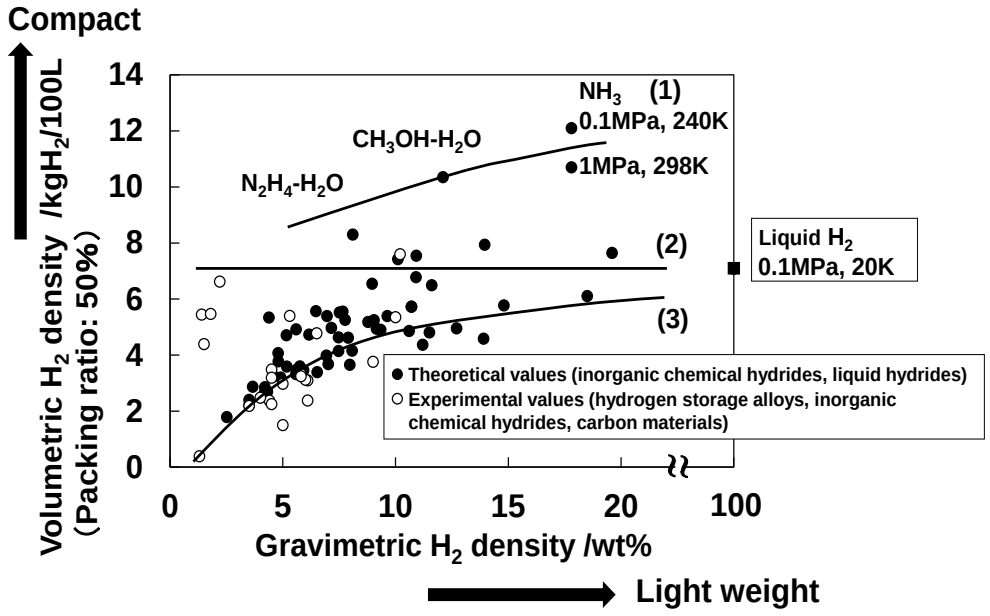

Figure 1.3.2 Gravimetric and volumetric H_2 densities of hydrogen storage materials such as hydrogen storage alloys, inorganic chemical hydrides, carbon materials and liquid hydrides [20].

used to produce mechanical work or heat [21]. Figure 1.3.3 shows the relation between the standard heat of formation and the reversible H_2 storage capacity of hydrogen storage materials. The standard heat of formation decreases with reversible hydrogen density without NH_3. The standard heat of formation of NH_3 is -30.6 kJ $mol^{-1}(H_2)$ [12]. This value almost satisfies the ΔH^0 (— 20 to —30 kJ $mol^{-1}(H_2)$) required for practical hydrogen storage materials [22].

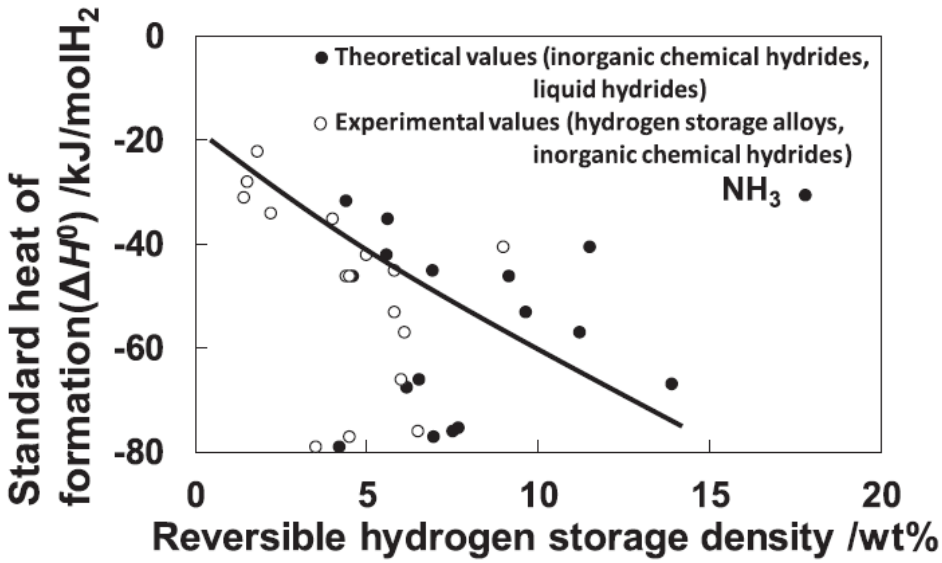

Figure 1.3.3 Standard heat of formation and reversible H_2 storage density of hydrogen storage materials such as hydrogen storage alloys, inorganic chemical hydrides and liquid hydrides [20].

Currently, the main method for producing hydrogen from renewable energy is to obtain hydrogen from water by electrolysis. The theoretical hydrogen conversion efficiency η is investigated by comparing the standard heat of formation for water (ΔH_h^0, higher heating value (HHV): 286 kJ /

mol(H_2)) [19] and hydrogen storage material (ΔH^0). The theoretical hydrogen conversion efficiency η is expressed by the following equation.

$$\eta = \frac{\Delta H_{\mathrm{h}}^0 - \Delta H^0}{\Delta H_{\mathrm{h}}^0} \qquad \text{(Equation 1.1)}$$

The theoretical hydrogen conversion efficiency η of NH_3 is 89.3% (η of C_7H_{14}: 76.4%, η of MgH_2: 73.7%) [19]. The efficiency is comparable that of conventional $LaNi_5$ alloy (88.8%) [21]. Therefore, ammonia can convert as much or more hydrogen energy than common hydrogen storage materials.

1.4 Ammonia

Ammonia is useful both as a hydrogen carrier and as a fuel. However, ammonia is a flammable substance and toxic. In order to utilize ammonia safety, it is important to consider the flammability and health hazard of ammonia. The regulations for the flammability and health hazard are defined in each region. The main standard regulations in each region are GHS (The Globally Harmonized System of Classification and Labelling of Chemicals) in Japan, NFPA (National Fire Protection Association) 704 in USA, and CLP (Classification, Labelling and Packaging of substances and mixtures) in Europe. The correlation between flammability and the properties of the hydrogen carriers was evaluated.

NFPA 704 is also known as "Fire Diamond" because of the diamond-shaped sign that it is used by emergency personnel to identify what to do in the accident of a spill, fire or other. Figure 1.4 shows fire diamonds of hydrogen carriers such as ammonia, liquid hydrogen and organic hydrides (toluene and methyl cyclohexane). The flash points of

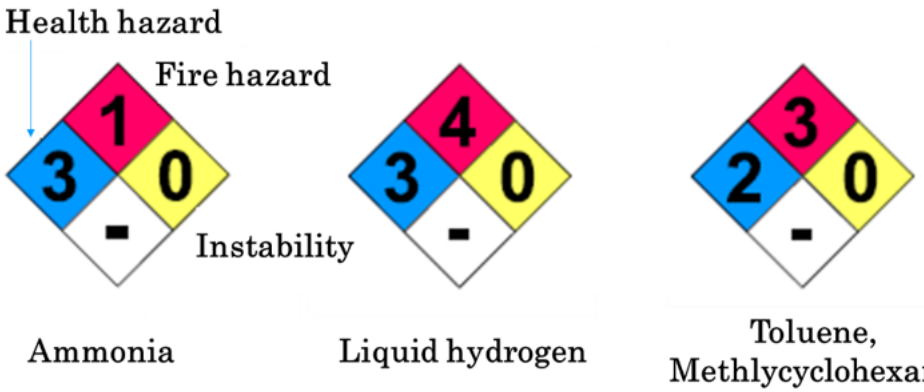

Figure 1.4 Fire diamond of ammonia, liquid hydrogen, toluene and methylcyclohexane as hydrogen carriers.

hydrogen carriers are 20 K for hydrogen, 267 K for organic materials, and 405 K for ammonia, respectively [23,24]. Therefore, NFPA flammability of ammonia is low value of 1. The CLP and Japanese GHS abilities also have similar trend, excluding the ammonia value of Japanese GHS. This is due to the fact that the flammability classification of Japanese GHS is defined by the explosive limit in air.

NFPA health hazard of ammonia has high value of 3 due to high solubility in water, corrosive and exothermic properties. NFPA health hazard of liquid H_2 has high value 3 because of suffocation death due to lack of oxygen and frostbite [25], which is the same as ammonia.

The NFPA health hazard of organic hydride (toluene and methyl cyclohexane) is 2. The CLP and Japanese GHS abilities of ammonia and organic hydrides also have similar trend.

Moreover, ammonia and toluene were compared by lethal concentration 50 (LC50). LC50 is a general indicator of an acute toxicity and is defined as the dose causing mortality in 50% of a group of animals during a predetermined period. The LC50 of ammonia and toluene are 7679 ppm and 7460 ppm (4 h rat inhalation), respectively [23]. Thus, it is assumed that the health hazards of these 3 kinds of liquid hydrogen carriers have same level.

Ammonia is less flammable than other hydrogen carrier materials, and its toxicity is almost the same. Therefore, ammonia is an important energy storage material because of its superiority as a hydrogen energy carrier and fuel utilization. However, humans detect ammonia at 1.5 ppm

[26]. American Conference of Governmental Industrial Hygienists (ACGIH) threshold limit value (TLV) for an 8 h time weighted average (TWA) exposure is 25 ppm (18 mg m^{-3}) [27]. Therefore, ammonia storage materials are becoming required for safety usage of ammonia.

1.5 Ammonia storage materials

Ammonia leaks account for 10% of all toxic and deleterious material leaks. All the accidents with NH_3 are caused by leaks from valve, pipe and flange in the plant facilities [28]. The maximum NH_3 vapor concentration accepted in an offensive odor control law at industrial area in Japan is 2 ppm (NH_3 vapor pressure: 0.2 Pa at atmospheric pressure) [29]. Therefore, the equilibrium NH_3 pressure (plateau pressure) is required to be lower than 0.2 Pa for the NH_3 storage materials as a remover, indicating that the NH_3 storage capacity should be large. NH_3 storage materials store NH_3 in the form of ammine [30], ammonium ion (NH_4^+) [31] and NH_3 molecule [32]. Metal halides and complex hydrides generally react with metal (cation) and NH_3 to form metal amine complex salts. Proton-based materials store NH_3 in the form of ammonium ion by the coordinate bond between proton of the materials and NH_3. Porous materials adsorb NH_3, and water dissolves NH_3 in the form of molecules.

Thermodynamic characterization is required for ammonia storage materials to understand the reaction with NH_3. Thermodynamic properties are analyzed based on the same theory as the metal-hydrogen system described in chapter 1.2.

Metal halides

Metal halides compose of metals and halogen elements are considered as the attractive NH_3 storage materials because they form metal ammine complex salts. NH_3 is coordinated to the metal and is called as a

ligand [30]. NH_3 absorption of metal halides are expressed by the following equation [30, 33-39].

$$MX_m + nNH_3 \rightarrow M(NH_3)_nX_m \quad \text{(Equation 1.2)}$$

M: Li, Na (m = 1), Mg, Ca, Mn, Co, Ni, Cu, Zn, Sr, Ba, Ag (m = 2), Co (m = 3), Pt (m = 4) etc., X: Cl, Br, I, n: 1, 2, 4, 6, 8, where n is coordination number.

NH_3 absorption properties of $MgCl_2$ have been studied because of its high NH_3 storage capacity of 52 wt%. Figure 1.5.1 shows experimental and calculated pressure composition isotherms for $MgCl_2$-NH_3 system [30,33]. At 293 K, $MgCl_2$ and NH_3 did not form mono- or di-ammine complexes, but hexa-ammine complexes. This suggests that a large activation barrier exists to form ammine complex salts with a low coordination number [33].

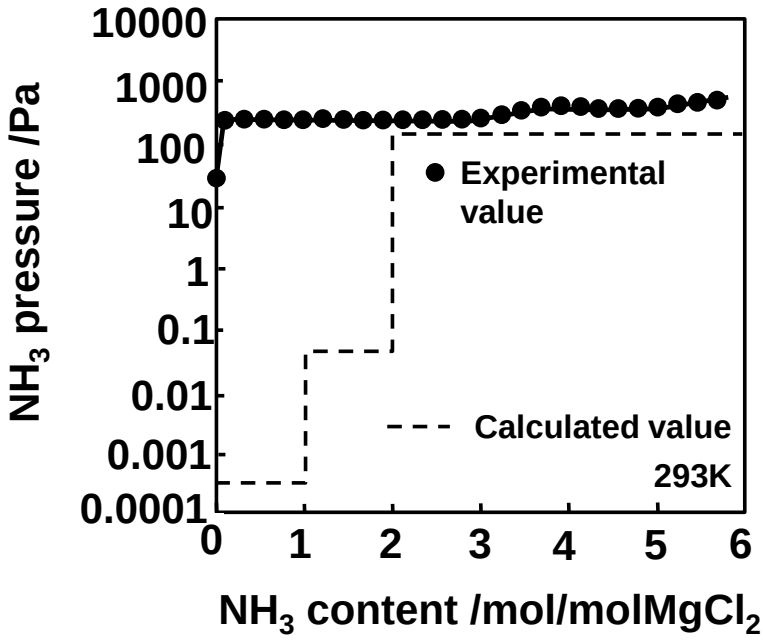

Figure 1.5.1 Ammonia pressure composition isotherms for $MgCl_2$[33,35,36]

Table 1.5.1 shows the theoretical gravimetric NH_3 density, plateau pressure in metal halide and NH_3 systems. The gravimetric NH_3 densities of metal ammine complex salts are 7-62 wt%. The ammonia equilibrium pressure of the metal halides is calculated from Equation 1.2.4 using ΔH^0 and ΔS^0. The calculated equilibrium pressure of metal ammine complex with the coordination number 1-2 is less than 0.2 Pa. Therefore, it is suggested that if the activation barrier is lowered by catalysts, metal halides become more useful.

Table 1.5.1 Theoretical gravimetric NH_3 density, plateau pressure of NH_3, and standard enthalpy and entropy change of metal halides absorbed NH_3

Metal halides	Ammonia storage /mol ratio	Gravimetric NH_3 density / wt%	Plateau pressure / Pa	Standard enthalpy change ΔH^0 / kJ $mol^{-1}(NH_3)$	Standard entropy change ΔS^0 / J $K^{-1}mol^{-1}(NH_3)$	Ref.
LiCl	4	61.6	178,000 (293 K)	-34	-119	34,37
NaI	5	36.2	55,000 (293 K)	-	-	34,37
$MgCl_2$	1	15.2	0.000645[a] (298 K)	-87	-135	35,36
	2	26.3	0.0804 (298 K)	-74.9	-135	35,36
	6	51.8	500 (293 K)	-55.6	-135	35,36
$CaCl_2$	1	13.3	1.36[a] (298 K)	-69	-138	35
	2	23.5	21.2[a] (298 K)	-63.2	-142	35
	4	38.5	40,300[a] (298 K)	-42.3	-134	35
	8	55.1	69,900[a] (298 K)	-41	-135	35
	8	55.1	22,000 (293 K)	-	-	34,37
$CaBr_2$	8	40.5	7,000 (293 K)	-	-	34,37
$MnCl_2$	1	11.9	0.0201[a] (298 K)	-84.1	-154	38
	2	21.3	31,000[a] (298 K)	-71.1	-154	38
	6	44.8	3370[a] (298 K)	-47.3	-149	38
$MnBr_2$	1	7.35	0.0236[a] (298 K)	-83.7	-150	38
	2	13.7	0.277[a] (298 K)	-77	-152	38
	6	32.2	3,370[a] (298 K)	-53.1	-154	38
$SrCl_2$	2	17.7	5,800[a] (298 K)	-58.9	-174	39
	8	46.2	50,800[a] (298 K)	-43.4	-140	39
$BaCl_2$	8	39.6	127,000 (293 K)	-37.7	-132	35,37

[a] Calculated value at 298 K from ΔH^0 and ΔS^0

Complex hydrides

Borohydrides, which is typical complex hydride, absorb NH_3 to form metal ammine complex salts as shown in the following equation [34,37,40-47].

$$M(BH_4)_m + nNH_3 \rightarrow M(NH_3)_n(BH_4)_m \quad \text{(Equation 1.3)}$$

where, M is Li, Na, Mg and Ca (n = 1-6, m = 3(Al), m = 2(Mg, Ca), m = 1(Li, Na)). NH_3 absorption and desorption reactions of sodium borohydride is reversible at room temperature [40,41] by the chemical reaction without hysteresis,

$$NaBH_4 + 2NH_3 \rightleftharpoons Na(NH_3)_2BH_4 \quad \text{(Equation 1.4)}$$

$NaBH_4$ can reversibly store 47 wt% of NH_3 under NH_3 plateau pressure of 90-96 kPa at 293 K [34,37,40,41]. KBH_4 shows no NH_3 absorption under 0.8 MPa NH_3 pressure (Table 1.5.2). $Mg(BH_4)_2$ and $Ca(BH_4)_2$ absorbed NH_3 are 57-2000 and 37-6500 Pa with multi step plateaus.

Table 1.5.2 shows the theoretical gravimetric NH_3 density, plateau pressure in borohydride and NH_3 systems. The gravimetric NH_3 densities of borohydride-NH_3 are 20-70 wt%. Aluminum borohydride reacts with NH_3 to form $Al(BH_4)_3$-$6NH_3$, and then NH_3 storage capacity is 59 wt%[42].

The NH_3 plateau pressures of metal borohydride ammine complex salts are above 30 Pa, which doesn't satisfy the regulation value of the odor control law at industrial area in Japan.

Figure 1.5.2(i) shows a pressure composition isotherm for $NaBH_4$-NH_3 system with NH_3 content from 0 to above 9 mol(NH_3) mol^{-1}($NaBH_4$). The NH_3 vapor pressure increases above the NH_3 content of 2 mol(NH_3) mol^{-1}($NaBH_4$). This behavior can be explained by the solubility of $NaBH_4$ in NH_3 (104 g($NaBH_4$) /100g(NH_3), NH_3 content: 2.1 mol(NH_3) mol^{-1}($NaBH_4$)) [43]. It is clarified by NMR and FTIR measurements that the NH_3 absorption state of $NaBH_4$ with NH_3 content of 0-9 mol(NH_3) mol^{-1}($NaBH_4$) is liquid[41]. From equation 1.2.4, in the NH_3 content from 0 to 2 mol(NH_3) mol^{-1}($NaBH_4$) state, c is 3 (NH_3 and $NaBH_4$) and p is 3 (gas(NH_3), liquid ($NaBH_4$-2NH_3) and solid ($NaBH_4$) phase), so f is 1. The pressure at equilibrium is constant because the temperature is fixed. Then, above the NH_3 content of 2 mol(NH_3) mol^{-1}($NaBH_4$) state, c is 2 (NH_3 and $NaBH_4$) and p is 2 (gas(NH_3), liquid($NaBH_4$-(2+x)NH_3) phase), so f is 2. The NH_3 vapor pressure changes above the NH_3 content of 2 mol(NH_3) mol^{-1}($NaBH_4$).

Ammonia borane (NH_3BH_3) is a typical complex hydride. Figure 1.5.2(ii) shows a pressure-composition isotherm for NH_3BH_3-NH_3 system [44]. Ammonia borane also absorbs 27 wt % of NH_3 at 105 Pa and 296 K. The NH_3 vapor pressure increases drastically above NH_3 content of 0.7 mol(NH_3) mol^{-1}(NH_3BH_3). This value corresponds to the solubility of NH_3BH_3 in liquid NH_3 (260 g(NH_3BH_3) / 100 g(NH_3), NH_3 content: 0.7 mol(NH_3) mol^{-1}(NH_3BH_3)). This indicates that NH_3BH_3 absorbed NH_3 is liquid [45].

Table 1.5.2 Theoretical gravimetric NH_3 density, plateau pressure of ammonia gaseous, and standard enthalpy and entropy change of complex hydrides-NH_3 system and NH_3 gas

Complex hydrides	Ammonia storge /mol ratio	Gravimetric NH_3 density / wt%	Plateau pressure / Pa	Standard enthalpy change ΔH^0 / kJ $mol^{-1}(NH_3)$	Standard entropy change ΔS^0 / J K^{-1} $mol^{-1}(NH_3)$	Ref.
$NaBH_4$	2	47.4	90,000 (293 K)	-29	-98	34,40,41
$LiBH_4$	1	43.9	1,000 (293 K)	-44.8		37,46
	3	70	4,000 (293 K)			37
	4	76	10,000 (293 K)			37
$Mg(BH_4)_2$	1	24	57 (293 K)			34,37
	2	38.7	96 (293 K)			34,37
	5	61.2	2,000 (293 K)			34,37
$Ca(BH_4)_2$	1	19.6	37 (293 K)	-52.7		34,37,47
	2	32.8	300 (293 K)	-48.0		34,37,47
	5	55	6,500 (293 K)	-34.9		34,37,47
$Al(BH_4)_3$	6	58.8				42
NH_3BH_3	0.7	27.9	100,000 (296 K)			44
NH_3 gas		100	850,000 (293 K)	-23	-97	34, 48

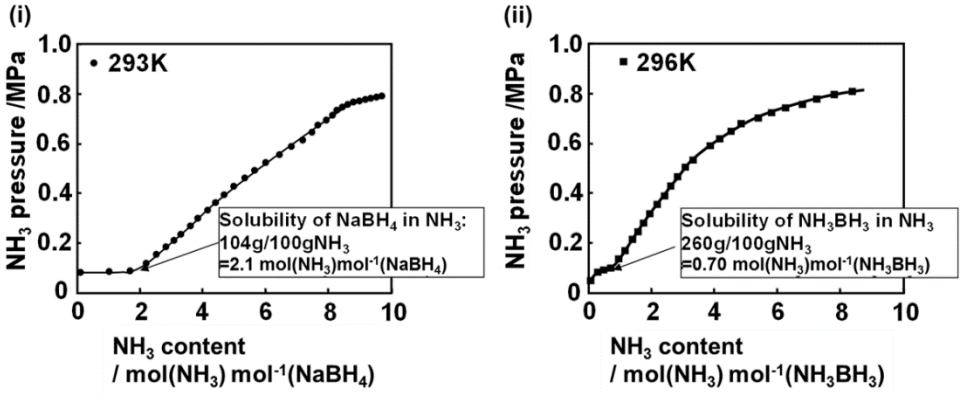

Figure 1.5.2 Pressure composition isotherms for (i)$NaBH_4$-NH_3 system and (ii)NH_3BH_3-NH_3 system [34,41,44]

Proton-based materials

Proton-based materials including H^+, reacts with lone electron pair of NH_3 in the atmosphere and in the ammonia water to form ammonium ion at room temperature [49-53] by the following equation

$$MH_n + nNH_3 \rightarrow M(NH_4)_n \quad \text{(Equation 1.5)}$$

Table 1.5.3 shows NH_3 densities, NH_3 equilibrium pressure, standard enthalpy change and entropy change of proton-based materials. The solid proton-based materials such as ammonium sulfate (NH_4HSO_4), acid impregnated charcoal, zirconium bis(mono-hydrogen phosphate) monohydrate [α-$Zr(HPO_4)_2 \cdot (H_2O)$] (α-zirconium phosphate, α-ZrP) absorb NH_3 below 0.2 Pa [31,49-51,53].

H^+ of proton-based material reacts with lone pair of NH_3 to form coordinate bond. This reaction is almost exothermic. The standard enthalpy changes ΔH^0 of the solid NH_4HSO_4 is -109 kJ $mol^{-1}(NH_3)$ [53]. The absolute values of the ΔH^0 are large compared with the metal halides and metal borohydrides. Moreover, the absolute value of the standard entropy change for the solid NH_4HSO_4 is 191 J $K^{-1}mol^{-1}(NH_3)$ and similar to the entropy of NH_3 gas (193 J $K^{-1}mol^{-1}(NH_3)$ at 298 K) [34,49]. The absolute values are large compared with metal halides and metal borohydrides. Therefore, it is suggested that proton-based materials stably absorb ammonia at low ammonia pressures compared to other materials.

Porous Materials

Porous materials have a high specific surface area and have the potential to adsorb large amounts of ammonia. Table 1.5.3 shows NH_3 densities, NH_3 equilibrium pressure and standard enthalpy change of porous materials. The adsorption isotherm for the activated carbon shows Langmuir type equation. By the Clausius-Clapeyron equation, the standard enthalpy changes on the activated carbon are estimated to be -8 to -17 kJ/ mol(NH_3) [54]. The adsorption of NH_3 gas on activated carbon is mainly based on physical adsorption (van der Waals forces) [54]. Therefore, the absolute value of standard enthalpy change is smaller than that of other ammonia storage materials. Zeolite also adsorbs NH_3 by electrostatic attraction. Thus, the standard enthalpy changes on the zeolite are -30 to -49 kJ/ mol(NH_3) [56].

Recently, prussian blue type materials are demonstrated to have high ammonia adsorption properties. Prussian blue shows 12.5 mmol / g of NH_3 capacity at 0.1 MPa [57]. Moreover, prussian blue type materials, Cobalt hexacyanocobaltate (CoHCC) and copper hexacyanoferrate (CuHCF), have the NH_3 capacities of 21.9 mmol/g and 20.2 mmol/g at 0.1 MPa, respectively. [57]. The gravimetric NH_3 densities of those porous materials are 0.1-27 wt%, as shown in Table 1.5.3.

Water

The ammonia storage capacity (solubility) of water greatly depends on the ammonia vapor pressure and temperature. For example, the gravimetric NH_3 density in NH_3 water is 32 wt% at 0.1 MPa and 298 K as shown in Table 1.5.3 [58]. The standard enthalpy change to form NH_3-H_2O

solution (32 wt%) is -30 kJ $mol^{-1}(NH_3)$ [59]. In the NH_3 water, positive charged $H^{\delta+}$ of H_2O and $N^{\delta-}$ of NH_3 form hydrogen bond [33]. Water is a NH_3 absorbent in the plant facilities [60] to decrease the leaked NH_3 concentration in the space because of the large solubility [58,59] and the large diffusion coefficient in water (1.5×10^{-5} cm^2 s^{-1} at 293 K) [53]. The large diffusion coefficient appears to be due to the low viscosity of water (1 mPa・s at 293 K) compared with the solid like glass (10^{14} Pa・s at 773 K) [61,62].

Table 1.5.3 Gravimetric NH_3 density, equilibrium pressure of gaseous ammonia, and standard enthalpy and entropy changes of proton-based materials, porous materials and water

Materials	Materials absorbed ammonia	Gravimetric NH_3 density / wt%	Equilibrium pressure / Pa	ΔH^0 / kJ mol^{-1} (NH_3)	ΔS^0/ J K^{-1} mol^{-1} (NH_3)	Ref.
$(NH_4)HSO_4$	$(NH_4)_2SO_4$	12.9	3.5×10^{-5} (298 K)[b] 4×10^{-7}-4×10^{-9}(298 K)	-109	-191	31,53
Acid imoregnated charcoal	-	3.2[a]	0.01 (298 K)	-	-	49
$Zr(HPO_4)_2$ H_2O	$Zr(NH_4PO_4)_2$ H_2O	10.2[a]	0.2 (293 K)	-	-	50,51
Activate carbons	-	0.39	10 (298 K) 50 (303 K)	-8 to -17	-	54,55
Sepiolite	-	2.4	-	-	-	55
Zeolite (Li-X)	-	5.0[a]	8 (293 K)	-30 to -49	-	56
Prussian blue cobalt	-	17.6[a]	100,000 (298 K)	-	-	49,57
Water	-	32	100,000 (298 K)	-30	-	58,59

[a] Experimental data [b] calculated value from ΔH^0 and ΔS^0

Figure 1.5.3 (i) shows the solubility of NH_3 in water as a function of temperature [58]. The solubility of NH_3 is high and 46 g / 100 g(H_2O) (32

wt%) at the NH_3 vapor pressure of 0.1 MPa and 298 K (Table 1.6). The vapor pressure decreases with temperature [58]. The NH_3 vapor concentration and the NH_3 concentration in the solution have similar high values at 298 K as shown in Figure 1.5.3 (ii) [60]. Here, the value of vapor concentration (ppm) is 10 times as large as the value of vapor pressure (Pa). This indicates that NH_3 vapor concentration corresponds to NH_3 concentration in NH_3 water at 298 K.

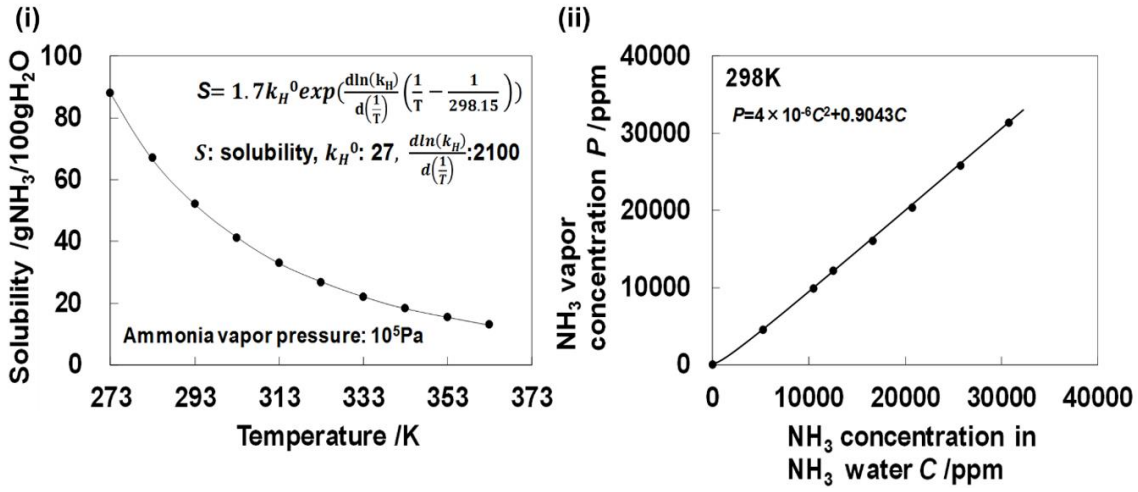

Figure 1.5.3 (i) Solubility of NH_3 in water vs temperature (ii) relation between NH_3 vapor concentration and NH_3 concentration in NH_3 water at 298 K. [58,59]

Figure 1.5.4 shows experimental and calculated equilibrium NH_3 vapor pressures of metal ammine complex salts, ammonium ion-based materials, porous materials ad/absorbed NH_3, NH_3 water and liquid NH_3. The NH_3 vapor pressure is classified into three categories: (1) NH_3 vapor pressure < 0.2 Pa, (2) 0.2 Pa < NH_3 vapor pressure < 1000 Pa, (3) 1000 Pa < NH_3 vapor pressure < 200,000 Pa. $Zr(NH_4PO_4)_2$,(H_2O), $(NH_4)_2SO_4$, NH_3

ad/absorbed impregnated charcoal, $Mg(NH_3)Cl_2$, $Mg(NH_3)_2Cl_2$, $Mn(NH_3)Cl_2$ and $Mn(NH_3)Br_2$ have low NH_3 vapor pressure of 0.2 Pa or below.

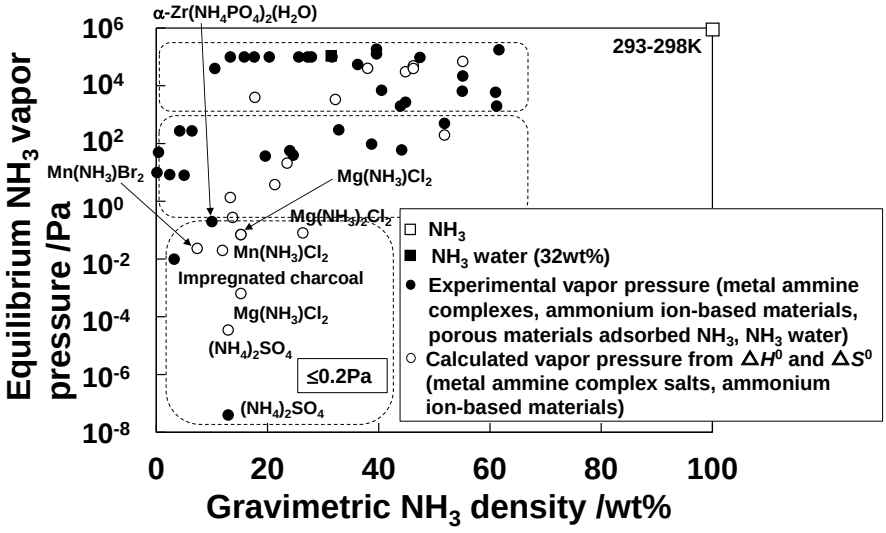

Figure 1.5.4 Equilibrium NH_3 vapor pressure and gravimetric NH_3 densities of ammonia storage materials [68].

The densities of $(NH_4)_2SO_4$, $Mg(NH_3)_6Cl_2$, $Mg(NH_3)_2Cl_2$, $Ca(NH_3)_8Cl_2$, $Mn(NH_3)_6Cl_2$, $Sr(NH_3)_8Cl_2$, $Ni(NH_3)_2Cl_2$, $Ni(NH_3)_2Br_2$, $Mn(NH_3)_2Cl_2$, $Mn(NH_3)_2Br_2$, $Mn(NH_3)_6Br_2$, α-$Zr(NH_4PO_4)_2 \cdot H_2O$ and NH_3 water (32 wt%) are 1.77 [53], 1.25 [63], 1.70 [37], 1.19 [63], 1.41 [63], 1.30 [64], 2.31 [65], 3.17 [65], 2.06 [38], 2.84 [38], 1.80 [38], 2.39 [66] and 0.89 [53,67] g cm^{-3}, respectively. These materials are classified as a solid or as a liquid. The volumetric NH_3 densities of solid materials are calculated by assuming that those packing ratio is 50%.

Figure 1.5.5 shows the volumetric and the gravimetric NH_3 densities of metal ammine complex salts, $(NH_4)_2SO_4$, α-$Zr(NH_4PO_4)_2 \cdot H_2O$ and NH_3

water. The volumetric NH_3 densities increase with the gravimetric NH_3 densities, approaching constant value of 0.33 kg(NH_3) L^{-1}. The volumetric NH_3 density of liquid ammonia is 0.603 kg(NH_3) L^{-1} at 298 K and 0.1 MPa. Therefore, a volume NH_3 density of about half is considered to be the limit for ammonia storage materials.

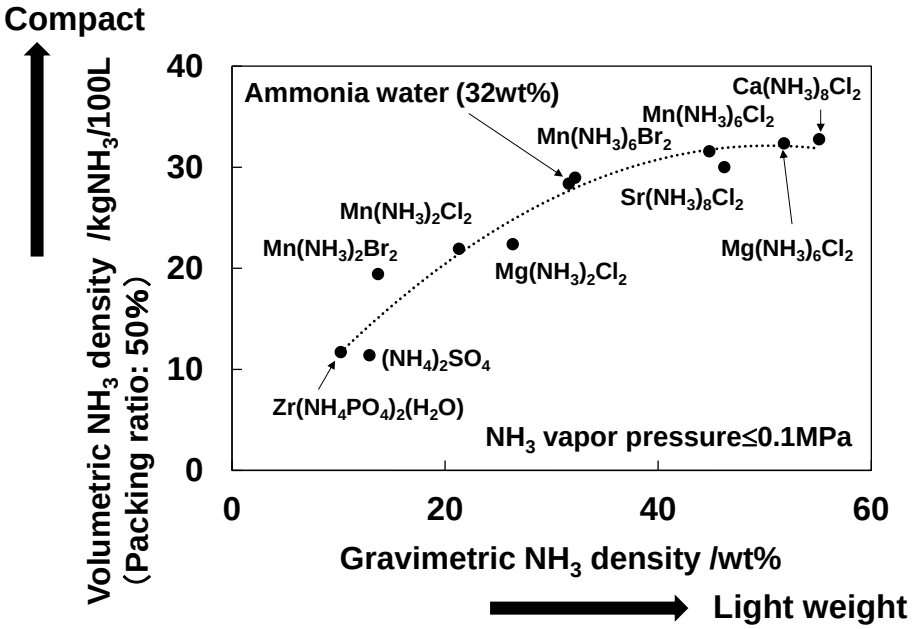

Figure 1.5.5 Gravimetric and volumetric NH_3 densities of ammonia storage materials such as metal ammine complex salts, $(NH_4)_2SO_4$, α-$Zr(NH_4PO_4)_2 \cdot H_2O$ and NH_3 water [68].

References

[1] Fossil fuel, Retrieved December 29th, 2020 from https://www.britannica.com/science/fossil-fuel

[2] N, Abas, A. Kalair, N. Khan, *Futures*, **69** (2015) 31-49.

[3] *Statistical Review of World Energy, 2020 | 69th edition*, bp p.l.c., page 4, Retrieved December 29th, 2020 from https://www.bp.com/content/dam/bp/businesssites/en/global/corporate/pdfs/energy-economics/statistical-review/bp-stats-review-2020-full-report.pdf

[4] History of the IPCC, Retrieved December 29th, 2020 from https://www.ipcc.ch/about/history/

[5] Adoption of the paris agreement, Retrieved December 29th, 2020 from https://unfccc.int/sites/default/files/english_paris_agreement.pdf

[6] G20 Riyadh Summit, Retrieved December 29th, 2020 from https://www.mofa.go.jp/ecm/ec/page6e_000220.html

[7] *New Energy Outlook 2020*, Bloomberg NEF, Retrieved December 29th, 2020 from https://about.bnef.com/new-energy-outlook/

[8] D. Gielen, F. Boshell, D. Saygin, M.D. Bazilian, N. Wagner, and R. Gorini, *Energy Strategy Reviews*, **24** (2019) 38-50.

[9] Renewable energy, Retrieved December 29th, 2020 from https://www.britannica.com/science/renewable-energy

[10] *Renewables 2020 Global Status Report*, REN21, page 31-34, Retrieved December 29th, 2020 from https://www.ren21.net/wp-content/uploads/2019/05/gsr_2020_full_report_en.pdf

[11] I. Hadjipaschalis, A. Poullikkas, and V. Efthimiou, *Renewable and Sustainable Energy Reviews*, **13** (2009) 1513-1522.

[12] H. A. Behabtu, M. Messagie, T. Coosemans, M. Berecibar, K.A. Fante, A.A. Kebede, and J.V. Mierlo, *Sustainability*, **12** (2020) 10511-10520.

[13] T.M. Gür, *Energy Environ. Sci.*, **11** (2018) 2696-2767.

[14] X. Luo, J. Wang, M. Dooner, and J. Clarke, *Applied Energy*, **137** (2015) 511-536.

[15] *Fuel Cell Technologies Office; Multi-Year Research, Development, and Demonstration Plan*, Energy Efficiency & Renewable Energy, page 3.3.9, page 3.3.11-14 and page 3.4.17-31, Retrieved December 29th, 2020 from https://www.energy.gov/eere/fuelcells/downloads/hydrogen-and-fuel-cell-technologies-office-multi-year-research-development

[16] *Hydrogen and Metal*, Y. Fukai, I. Tanaka, and Y. Uchida, Uchida Rokakuho

Publishing Co. Ltd.
[17] Z.P. Li, H. Liu, K. Arai, N. Morigazaki, and S. Suda, *Journal of Alloys and Compounds*, **356-357** (2003) 469-474.
[18] K. Mizuuchi, T. Takeuchi, M. Fukusumi, M. Sugioka, and H. Nagai, *J. Japan Inst. Metals*, **62** (1998) 893-898.
[19] *CRC handbook of Chemistry and physics. 84th ed.*, D.R. Lide, CRC Press, 2003-2004.
[20] Y. Kojima, *Int. J. hydrogen energy*, **44** (2019) 18179-18192.
[21] ISO 13600:1997(en) Technical energy systems - Basic concepts, Retrieved December 29th, 2020 from https://www.iso.org/obp/ui/#iso:std:iso:13600:ed-1:v1:en
[22] Y. Kojima, *Materia Jpn.*, **52** (2013) 333-336.
[23] Workplace safety site. Ministry of Health, Labour and Welfare, Japan, Retrieved December 29th, 2020 from
(i)ammonia http://anzeninfo.mhlw.go.jp/anzen/gmsds/7664-41-7.html
(ii)methylcyclohexane http://anzeninfo.mhlw.go.jp/anzen/gmsds/0977.html
(iii)toluene http://anzeninfo.mhlw.go.jp/anzen/gmsds/108-88-3.html.
[24] Hydrogen fundamentals., Retrieved December 29th, 2020 from http://www.hysafe.org/download/997/brhs_ch1_fundamentals-version%201_0_1.pdf.
[25] Cameo Chemicals. Hydrogen, refrigerated liquid (cryogenic liquid). CAS Number 1333-74-0, Retrieved December 29th, 2020 from https://cameochemicals.noaa.gov/chemical/3606.
[26] Measurement of Odor Threshold by Triangle Odor Bag Method. Ministry of the Environment, Japan, Retrieved December 29th, 2020 from https://www.env.go.jp/en/air/odor/measure/02_3_2.pdf
[27] The Fertilizer Institute, Nourish, Replenish Grow. Health effects of ammonia., Retrieved December 29th, 2020 from http://www.tfi.org/sites/default/files/documents/HealthAmmoniaFINAL.pdf.
[28] Y. Kojima, H. Ikeda. 28th annual meeting of the Japan institute of energy tournament; August 7, 2019 (Wednesday) to 8 (Thursday) Osaka.
[29] Odor control law in Japan, Retrieved December 29th, 2020 from http://www.pref.toyama.jp/sections/1103/reiki_int/reiki_honbun/i001RG00000429.html
[30] F.Basolo, R.C. Johnson, *Shriver and Atkins. Inorganic chemistry, 5th revised Edition.*, Oxford University Press; 2010. Science Reviews Limited, 1986.
[31] W.D. Scott, F.C.R. Cattell, *Atmos Environ.*, **13** (1979) 307-317.
[32] T. Asada, T. Ohkubo, K. Kawata, K. Oikawa, *J. Health Sci.*, **52** (2006) 585-589.

[33] T. Aoki, H. Miyaoka, H. Inokawa, T. Ichikawa, Y. Kojima, *J. Phys. Chem. C*, **119** (2015) 26296-26302.

[34] T. Aoki, T. Ichikawa, H. Miyaoka, Y. Kojima, *J. Phys. Chem. C*, **118** (2014) 18412-18146.

[35] C.Y. Liu, K. Aika. *Bull. Chem. Soc. Jpn.*, **77** (2004) 123-131.

[36] T.D. Elmøe, R.Z. Sørensen, U. Quaade, C.H. Christensen, J.K. Nørskov, T. Johannessen, *Chem. Eng. Sci.*, **61** (2006) 2618-2625.

[37] T. Zhang, H. Miyaoka, H. Miyaoka, T. Ichikawa, Y. Kojima, *ACS Appl. Energy Mater.*, **1** (2018) 232-242.

[38] H Reardon, J.M. Hanlon, M. Grant, I. Fullbrook, D.H. Gregory, *Crystals*, **2** (2012) 193-212.

[39] S. Lysgaard, A.L. Ammitzbøll, R.E. Johnsen, P. Norby, U.J. Quaade, T. Vegge, *Int. J. Hydrogen Energy*, **37** (2012) 18927-18936.

[40] Y. Kojima, T. Aoki, H. Miyaoka, H. Miyaoka, T. Ichikawa, 35th annual meeting of hydrogen energy systems society of Japan, December 3 (thursday) to 4 (friday) 2015, Tokyo.

[41] K. Nakajima, H. Miyaoka, K. Kojima, T. Ichikawa, Y. Kojima, *Chem. Commun.*, **55** (2019) 2150-2153.

[42] Y. Guo, X. Yu, W. Sun, D. Sun, W. Yang, *Angew. Chem. Int. Ed.*, **50** (2011) 1087-1091.

[43] J. Walbridge. *Prog. Inorg. Chem.*, **11** (1970) 99-231.

[44] H. Kawauchi, K. To, Y. Kojima, T. Ichikawa, Ammonia storage and release material, ammonia storage and release device, and exhaust gas purification system. 2014. p 43359.

[45] F.H. Stephens, V. Pons, R.T. Baker. *Dalton Trans.*, **25** (2007) 2613-2626.

[46] E.A. Sullivan, S. Johnson, *J. Phys. Chem.*, **63** (1959) 233-238.

[47] H. Chu, G. Wu, Z. Xiong, J. Guo, T. He, P. Chen, *Chem. Mater.*, **22** (2010) 6021-6028.

[48] NIST Chemistry WebBook. SRD 69, thermophysical properties of ammonia, Retrieved December 29th, 2020 from https://webbook.nist.gov/cgi/fluid.cgi?ID¼C7664417&Action¼Page.

[49] H. Nishino. *Environ. Technol. Jpn.*, **19** (1990) 643-645.

[50] M. Tsuhako, H. Nakayama, *J. Soc. Inorg. Mater. Jpn.*, **7** (2000) 679-684.

[51] Y. Kojima, Final report, emergency ammonia adsorption method, cross-ministerial strategic innovation promotion Program (SIP), “energy carrier”, Japan. March 31. 2019, April 2018. Y. Kojima, M. Yamaguchi, T. Ichikawa, H. Miyaoka. Proton-based

ammonia storage materials for nitrogen recycling hydrogen and energy carriers. Abstract of Papers.2019 Frontiers in Materials Processing, Application, Research & Technology (2019 FiMPART), Ahmedabad, India, December 15 (Monday) to 18 (Wednesday), 2019, https://www.jst.go.jp/sip/k04.html.

[52] M. Turco, P. Ciambelli, G. Bagnasco, A. LaGinestra, P. Galli, C. Ferragina, *J. Catal.* **117** (1989) 355-361.

[53] W.M. Haynes, *CRC handbook of chemistry and physics. 97th ed.*, CRC Press; 2016-2017.

[54] F.H. Stephens, V. Pons, R.T. Baker, Dalton Trans., **15** (2007) 2613-2626.

[55] H.Nishino, *Environ. Technol. Jpn.*, 19 (1990) 643-645.

[56] T. Miyoshi, K. Boki, S. Tanada, *Jpn. J. Ind. Health.*, **19** (1977) 87-91.

[57] A. Takahashi, H. Tanaka, D. Parajuli, T. Nakamura, K. Minami, Y. Sugiyama, Y. Hakuta, S. Ohkoshi, T. Kawamoto, *J. Am. Chem. Soc.*, **138** (2016) 6376–6379

[58] NIST Chemistry WebBook. SRD 69, Retrieved December 29th, 2020 from https://webbook.nist.gov/cgi/cbook.cgi?ID¼C7664417&Mask¼10.

[59] The Society of Chemical Engineers, *Chemical engineering handbook, rev. 6 Edition.*, Japan, Maruzen Co., Ltd., 1999, p. 81

[60] Ministry of Economy. Trade and industry, about the operation of the functional standards of the general high pressure gas safety regulations, Ministry of Economy, Trade and Industry, Agency for Natural Resources and Energy, Nuclear Safety and Security Bureau. NISA 69-70, Retrieved December 29th, 2020 from https://www.meti.go.jp/policy/tsutatsutou/tuuti1/TS1-1.pdf.

[61] A. Einstein, *Ann. Phys.*, **17** (1905) 549-560. Retrieved December 29th, 2020 from http://www.slab.phys.nagoya-u.ac.jp/uwaha/einstein1.pdf.

[62] A. Napolitano, E.G. Hawkins, *J. Res. Natl. Bur. Stand. A Phys. Chem.*, **68A** (1964) 439-448.

[63] R.Z. Sørensen, J.S. Hummelshøj, A. Klerke, J.B. Reves, T. Vegge, J.K. Nørskov, *J. Am. Chem. Soc.*, **130** (2008) 8660-8668.

[64] G. Fulks, G.B. Fisher, K. Rahmoeller, M.C. Wu, E. D'Herde, J. Tan, *A review of solid materials as alternative ammonia sources for lean NOx reduction with SAE Int*, SAE Technical Papers. April 2009, Paper No. 2009-01-0907.

[65] A. Leineweber, H. Jacobs, *J. Solid State Chem.*, **152** (2000) 381-387.

[66] A. Clearfield, J.M. Troup, *J. Phys. Chem.*, **77** (1973) 243-247.

[67] Specific gravity of aqua ammonia. Inyo Process, Retrieved December 29th, 2020 from https://inyoprocess.com/images/chem_appl/aqua_ammonia_specific_gravity_chart.pdf.

[68] Y. Kojima, M. Yamaguchi, *Int. J. Hydrogen Energy*, **45** (2020) 10233-10246.

2. Purpose

Among ammonia storage materials, water easily collects gaseous ammonia because of the large solubility and diffusion coefficient in water [1]. However, the ammonia equilibrium vapor pressure in water is proportional to the ammonia concentration (ammonia absorption) [2,3]. Therefore, by combining water with an ammonia storage material, it would be possible to make an ammonia removal system that has the absorption speed of water and the low concentration of ammonia in water and gas.

In this thesis, we focus on the following topics; (i) ammonia ad/absorption characteristics of insoluble proton-based solid acids, and (ii) thermodynamic and structural analyses of zirconium phosphate absorbed ammonia.

(i) Ammonia ad/absorption characteristics of insoluble proton-based solid acids

The measurements of ammonia equilibrium concentration and ammonia storage capacity are important to evaluate the ammonia removal property of materials in ammonia gas. However, from the ammonia water, the ammonia storage capacity and the ammonia equilibrium concentration of materials has not been reported yet.

In this study, insoluble proton-based solid acids are focused on as materials to be combined with water. Then, the ammonia storage capacity and the equilibrium concentration of insoluble proton-based solid acids are measured. The new ammonia removal system is estimated as an ammonia

remover for simulated leaked ammonia gas.

This result is taken up in section 1,2, and 6 of chapter 4 (4.1,2,6).

(ii) Thermodynamic and structural analyses of zirconium phosphate absorbed ammonia

Thermodynamic analysis

It was measured that zirconium phosphate ($Zr(HPO_4)_2$-H_2O, ZrP) has a large ammonia storage capacity (10.2 wt%) and a low ammonia concentration (below 1 ppm) in water. ZrP has a layered structure, and it is known that the crystal structure change before and after ammonia absorption ($Zr(HPO_4)_2 \cdot H_2O$ and $Zr(NH_4PO_4)_2 \cdot H_2O$) [4,5]. Therefore, the plateau region could be confirmed during ammonia absorption. Then, the thermodynamic properties could be analyzed by measuring the plateau region. However, there have been no research.

In this study, the ammonia plateau concentrations of ZrP at different temperatures are measured by temperature dependence of ammonia concentration composition isotherm (CCI) measurements. Then, thermodynamic properties such as the standard enthalpy change (standard heat of formation: ΔH_w^0) and standard entropy change (ΔS_w^0) of the ammonia absorption state of ZrP in ammonia water are calculated.

This result is taken up in section 3 of chapter 4 (4.3).

Structural analysis

The ammonia CCI of ZrP showed two levels of ammonia plateau equilibrium pressure. Therefore, it is possible that there are two ammonia absorption states of ZrP. However, fine structure (interlayer distance) and local structure (interlayer structure) of the ammonia absorption states of ZrP is not clarified.

In this section, we characterize the fine structure and local structure of the ammonia absorption states of ZrP using powder X-ray diffraction (pXRD), ^{31}P solid-state magic angle spinning nuclear magnetic resonance (solid-state MAS NMR), and Fourier transform infrared (FTIR) spectroscopy.

This result is taken up in section 4 and 5 of chapter 4 (4.4,5).

References

[1] Y. Kojima, and H. Ikeda, 4-5-3 safety of ammonia as hydrogen and energy carriers. Abstract of papers. 28th annual meeting of the Japan institute of energy tournament; August 7-8, 2019, Osaka.

[2] NIST Chemistry WebBook, Thermophysical Properties of Ammonia, Retrieved December 29th, 2020 from https://webbook.nist.gov/cgi/fluid.cgi?ID=C7664417 &Action=Page

[3] *Chemical Engineering Handbook, rev. 6 Edition*, The Society of Chemical Engineers, Maruzen Co., Ltd., 1999, page 81.

[4] L. Sedlakova, and V. Pekarek, *J. Less-Common Met.*, **10** (1966) 130-132.

[5] A. Clearfield, and J. M. Troup, *J. Phys. Chem.*, **77** (1973) 243-247.

3. Experiments

3.1 Materials

Pristine materials in this study are shown in Table 3.1. All proton-based materials and phosphates were used as received without further purification. Proton substitution of montmorillonite was carried out in hydrochloric acid [1]. Various concentrations of ammonia water were prepared by 10 wt% ammonia water and ion exchange water. After heat treatment about 150 ℃, KBr were handled in a glovebox purified by a gas recycling purification system (MP-P60W manufactured by Miwa MFG Co., Ltd.) to minimize influence of water in the air. Water level was kept below 0.1 ppm in the glove box.

Table 3.1 General information of materials

Materials	Company	purity, state
Calcium hydrogen phosphate dihydrate $Ca(HPO_4)\cdot 2H_2O$	Nacalai Tesque, Inc.	>98%, powder
Magnesium hydrogen phosphate trihydrate $Mg(HPO_4)\cdot 3H_2O$	Sigma Aldrich	>97%, powder
Montmollonite Kunipia F	Kunimine Industries	Powder
Impregnated AC granular Shirasagi GTSX4/6G	Osaka Gas Chemicals Co., Ltd.	Grain
Y type zeolite HSZ-331HSA	Tosoh	Powder
Mordenite type zeolite HSZ-620HOA	Tosoh	Powder
α-Zirconium phosphate $Zr(HPO_4)_2\cdot H_2O$ CZP-100	Daiichi Kigenso Kagaku Kogyo Co., Ltd.	Powder
HCl solution	Nacalai Tesque Inc.	35-37 %, solution
Standard ammonia Orion 951202	Thermo scientific	Solution
Ammonia water	KENEI Pharmaceutical Co., Ltd.	9.5~10.5 wt%, solution
NH_4Cl	Sigma Aldrich	>99%, powder
NaOH	Nacalai Tesque, Inc.	>97%, grain
Standard buffer solution	Nacalai Tesque, Inc.	pH 4.01, 6.86, 9.08, 10.02
Phosphoric acid H_3PO_4	Nacalai Tesque, Inc.	>85%, solution
KBr	Sigma Aldrich	>99%, powder

3.2 Ammonia ad/absorption measurement

3.2.1 Materials ad/absorbed ammonia in water

Ammonia has two kinds of forms which are NH_3 and NH_4^+ in ammonia water. For ammonia ad/absorption on materials, the concentration of NH_3 and NH_4^+ in water should be evaluated. NH_3 concentration ($[NH_3]$) was measured by the ammonia meter. Then, NH_4^+ concentration ($[NH_4^+]$) was calculated using the following equation 3.2.1,

$$[\mathrm{NH_4^+}] = \frac{\mathrm{K_b}}{10^{\mathrm{pH}-14}}[\mathrm{NH_3}] \qquad \text{(Equation 3.2.1)}$$

where K_b is the base dissociation constant and pH is the potential of hydrogen [2]. Then, the ammonia ad/absorption capacity (ammonia storage capacity; C_{st}) was calculated using the following equation 3.2.2,

$$C_{\mathrm{st}} = ([\mathrm{NH_3}]_{\mathrm{af}} + [\mathrm{NH_4^+}]_{\mathrm{af}} - [\mathrm{NH_3}]_{\mathrm{be}} + [\mathrm{NH_4^+}]_{\mathrm{be}}) \times L \qquad \text{(Equation 3.2.2)}$$

where $[NH_3]_{be}$ and $[NH_3]_{af}$ are NH_3 concentration before and after material is added, $[NH_4^+]_{be}$ and $[NH_4^+]_{af}$ are NH_4^+ concentration before and after material is added and L is the volume of ammonia water.

Moreover, nitrogen concentrations in the water are also checked to investigate whether it causes health hazards to organisms and environmental pollution such as red tide. Generally, the nitrogen concentration from ammonia is described as NH_3-N or NH_4-N. NH_3-N represents the nitrogen content of the NH_3, NH_4-N is the nitrogen content of the NH_4^+. In Japan, the nitrogen concentration derived from ammonia is

multiplied by 0.4 and compared to the reference value [3]. In this article, the nitrogen concentration ([N], ppm) was calculated using the following equation 3.2.3,

$$[N] = ([NH_3]/M_{NH3} + [NH_4^+]/M_{NH4+}) \times M_N \quad \text{(Equation 3.2.3)}$$

where M_{NH3}, M_{NH4+} and M_N are the molar mass of NH_3, NH_4^+ and N.

Procedure

The ammonia concentration and the potential of hydrogen (pH) in ammonia water were measured using ammonia meter (Orion Star A324 and Orion 9512 manufactured by Thermo Scientific Orion) and pH meter (CyberScan pH310 manufactured by EUTECH Ins.). The pH meter was corrected using four standard buffer solutions. A standard solution for ammonia meter was prepared by the following procedure. In a glove box, 157 mg of NH_4Cl was measured out, and then 50 ml of diluted water was added to the solution under air. NaOH was added to the solution to bring the pH above 12. This solution was used as the NH_3 standard solution containing 1000 ppm (NH_3), and then 5 ml of the solution was taken out and added 45 ml of diluted water. This process was repeated to prepare solutions up to 0.1 ppm. The ammonia meter was corrected using these NH_3 standard solutions.

50 ml of ammonia water (the initial ammonia concentration ($[NH_3]_{be}$) is about 2500 ppm) was prepared, and the temperature of the

solution was set to about 298 K by a water bath (Water bath BM-401, manufactured by Yamato Scientific Co., Ltd.). Then, 0.5 g of materials was added to the solution and the NH_3 concentration and pH were continuously measured at regular time intervals. After the change in NH_3 concentration subsides, the ammonia storage capacity was calculated by equation 3.2.2.

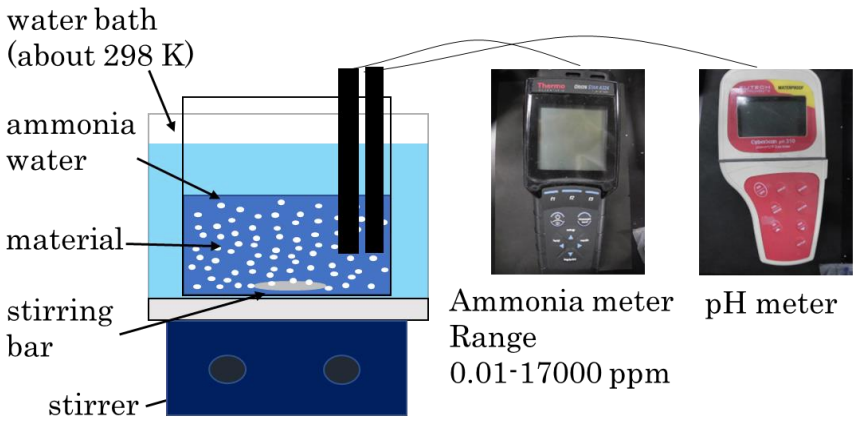

Figure 3.2.1 ammonia ad/absorption measurement

3.2.2 Ammonia concentration composition isotherm (CCI)

The ammonia concentration composition isotherm (CCI) measurements are a technique to know the relation between the ammonia concentration in water and the amount storage capacity for materials at an arbitrary temperature. Since the measurement is performed after waiting for a sufficient amount of time, it is considered to exist in an equilibrium state.

Henry's law is a gas law that states "when a dilute solution containing a volatile solute is in equilibrium with the gas phase, the pressure P of the solute is proportional to mole fraction of ammonia c_m." Then the following

equation is obtained.

$$\frac{P}{\mathrm{P_0}} = Kc_m \qquad \text{(Equation 3.2.4)}$$

where P_0 is 0.1MPa. Figure 3.2.2 shows the relative NH_3 vapor pressure P/P_0 as a function of mole fraction of NH_3 in the water solution. The NH_3 vapor pressure linearly increases with the mole fraction of ammonia at the constant temperature. It is indicated that Henry's law and the equation holds. Temperature dependence of K obtained by the slope in the figure is expressed by the equation

$$ln\,\mathrm{K} = \frac{\Delta H_s}{\mathrm{R}T} - \frac{\Delta S_s}{\mathrm{R}} \qquad \text{(Equation 3.2.5)}$$

where ΔH_s and ΔS_s is the heat of dissolution and entropy change by dissolution. Substituting equations 3.2.4 and 3.2.5 into equation 1.2.3,
The following equation is obtained.

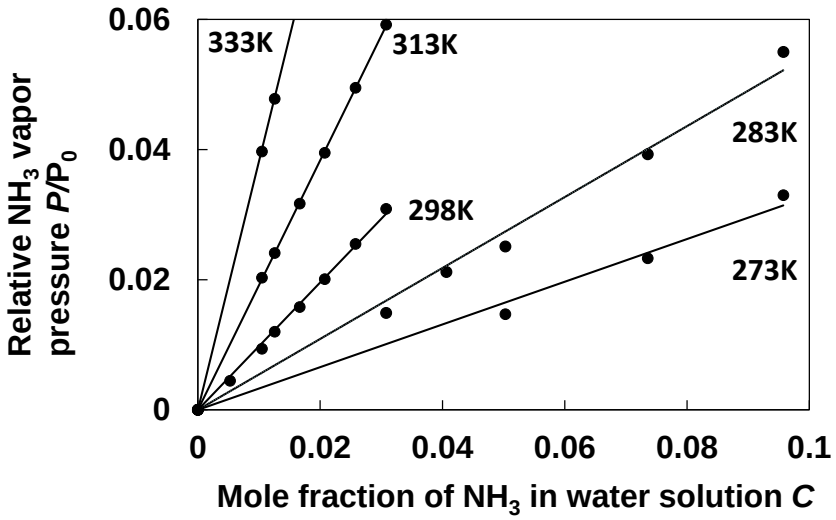

Figure 3.2.2 NH_3 vapor pressure vs mole fraction of NH_3 [4]

$$ln\, c_m = \frac{\Delta H^0 + \Delta H_s}{\mathrm{R}T} - \frac{\Delta S^0 + \Delta S_s}{\mathrm{R}}$$ (Equation 3.2.6)

Figure 3.2.3 shows van't Hoff plot of ammonia water. From the slope and the intercept, ΔH_s and ΔS_s are -30.9 kJ $mol^{-1}(NH_3)$ and -104 J K^{-1} $mol^{-1}(NH_3)$, respectively.

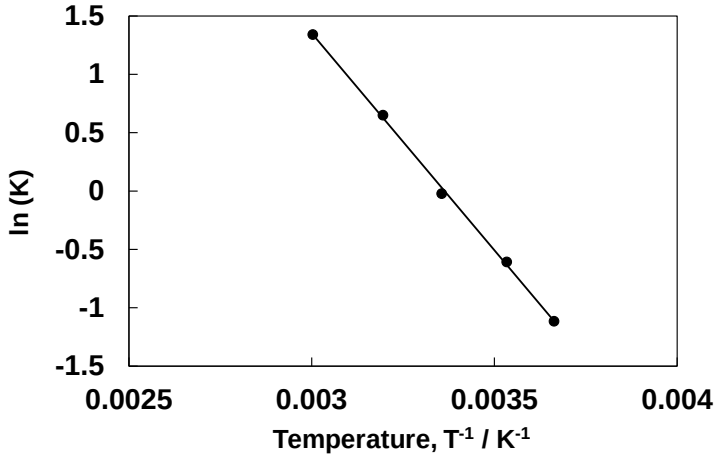

Figure 3.2.3 van't Hoff plot of ammonia water

These values are substituted into equation 3.2.7,

$$ln\, c_m = \frac{\Delta H^0 + 30900}{RT} - \frac{\Delta S^0 + 104}{R}$$ (Equation 3.2.7)

Procedure

The ammonia concentration and the potential of hydrogen (pH) in ammonia water were measured using the ammonia meter (Orion Star A324 and Orion 9512 manufactured by Thermo Scientific Orion) and the pH

meter (CyberScan pH310 manufactured by EUTECH Ins.). The ammonia meter and pH meter were corrected as in the procedure 3.2.1.

Ammonia water (50 ml) having various concentration was prepared, and the temperature of the solution was set to about 277, 298 or 313 K by a constant temperature of water bath (Water bath BM-401, manufactured by Yamato Scientific Co., Ltd.). The temperature of 277 K was controlled using ice. Then, 0.5 g of materials was added to the solution and the NH_3 concentration and the pH were continuously measured at the regular time intervals. After the change in NH_3 concentration subsides, we summarize the ammonia concentration in the solution and the ammonia storage capacity was calculated by equation 3.2.2.

3.3 Powder X-ray diffraction (pXRD)

X-ray diffraction is a technique for structural analysis and quantitative evaluation. The information obtained depends on states of materials. For powder materials, it is possible to identify and quantify the constituent phases, and analyze crystal size and crystallinity. X-ray are radio waves with wavelengths even shorter than ultraviolet light. The wavelength of the X-rays used in the measurement is typically about 0.5 to 2.5 Å, which corresponds to the atomic scale. When X-ray are irradiated on materials, some are scattered, some are absorbed and some are transmitted. Scattered X-rays are divided into two types: those with the same energy as the irradiated X-rays (elastic scattering; Thomson scattering) and those with a different energy (inelastic scattering; Compton scattering). If the atoms are regularly arranged in the material, the scattered X-rays strengthen each other at specific angles due to interference. This phenomenon is called diffraction. Figure 3.3 shows a schematic image of X-ray diffraction.

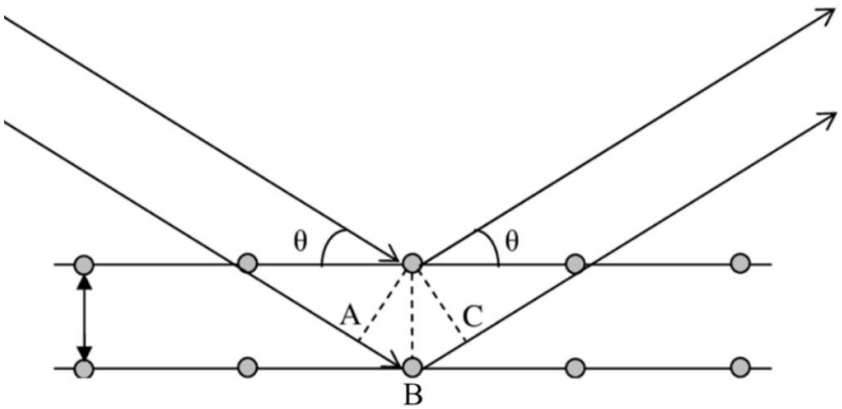

Figure 3.3 Diffraction of X-ray from lattice planes in the crystal [5]

If the phases of the scattered X-ray waves match, the scattered X-ray strengthen each other. Here, the lattice plane spacing is d and the angle of incidence of X-rays is θ. The line path difference between the neighboring planes (AB+BC) is $2d\sin\theta$. Therefore, when $2d\sin\theta$ is an integral multiple of the X-ray wavelength, the condition is that the scattered X-rays strengthen each other and diffraction occurs. Therefore, the conditions for the diffraction are expressed as follows.

$$2d\sin\theta = n\lambda \qquad \text{(Equation 3.3)}$$

where n is an integer and λ is the wavelength of the X-ray. This equation is known as Bragg's law.

The X-ray diffraction pattern obtained by pXRD is expressed as diffraction angle (2θ) on the horizontal axis and diffraction intensity (counts per seconds, cps) on the vertical axis. The diffraction angle depends on the lattice spacing of the material. The diffraction intensity depends on the arrangement of atoms and molecules and their species. The width of the peak is determined by the size of the crystallite and crystal distortion. The shape of the X-ray diffraction pattern depends on the crystal structure. Therefore, qualitative analysis of powder X-ray diffraction identifies the crystalline phase by comparing the measured diffraction patterns with those of known materials.

Procedure

Interlayer distance and intralayer structure of ZrP and ZrP absorbed ammonia were characterized by the pXRD measurement (Rigaku, RINT-2500V). ZrP and ZrP absorbed ammonia were dried vacuum overnight at room temperature. Each sample was pressed at a constant load on a glass holder before the XRD measurements. The X-ray source was Cu-Kα (λ = 1.54 Å) and the energy output was 8 kW (40 kV and 200 mA). The obtained XRD patterns were analyzed by the PDXL software with powder diffractions files (PDF) in the databases [ICDD, JICST, COD2019].

3.4 Thermogravimetry-Differential Thermal Analysis and Mass Spectrometry (TG-DTA-MS)

Thermogravimetry-differential thermal analysis and mass spectrometry (TG-DTA-MS) is a technique to estimate a reaction of a material and what gases are produced at each reaction temperature. It evaluates the weight change, differential heat and mass of volatile components produced by heating.

Figure 3.4.1 shows a schematic diagram of the TG-DTA system. Ar gas is flowing in the TG-DTA system. When the material is heated, gases are desorbed from the material. The desorbed gases cause weight loss of the material, which is measured as a weight difference between a sample and a reference under elevated temperature conditions. The desorbed gases are transferred with Ar gas as a carrier gas. Therefore, partial pressure of gases desorbed from the sample is removed, indicating that the inside of the furnace is realizing relatively low partial pressure of gases desorbed gas. The desorbed gases flow through the capillary and are directed to the mass

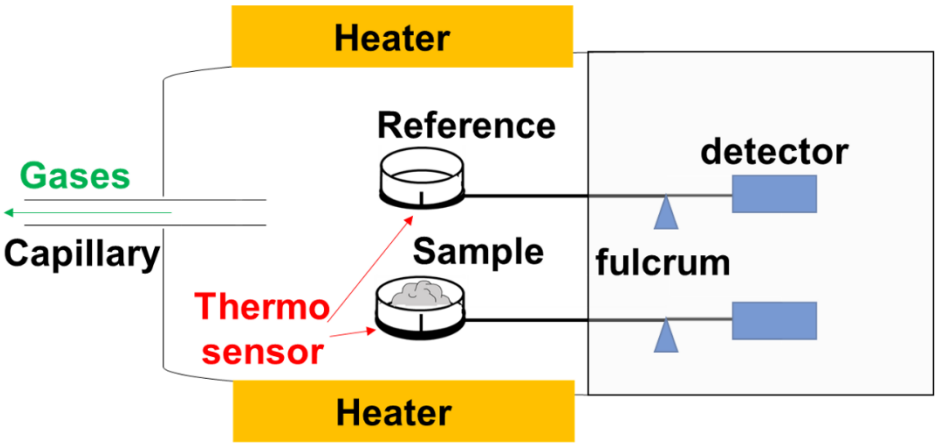

Figure 3.4.1 a schematic diagram of the TG-DTA system

spectrometer (MS).

Then, a thermo-sensor attached to the balance continuously records the temperature difference between the reference and the sample. This measurement can detect the heat flow due to the gases desorption or a phase transition of the material.

The gases desorbed from the sample can be identified by the MS measurements. Figure 3.4.2 shows a schematic diagram of the MS system. The apparatus is composed of three parts, an ionization source, a quadruple mass spectrometer, and a detector. The desorbed gases from the material are ionized by confliction with electron beam in ionization part. Thus, the ionized gas molecules can be expressed m/z, where m is mass of ionized gas molecules, z is charge number. If generated molecular ions have excess internal energy, the ions split into fragment ions. Molecular or fragment ions are perturbed as they enter the mass separator, where two sets of diagonal rods are energized with DC voltage and AC at radio frequency, and move in the direction of the arrow with complex oscillations. By adjusting

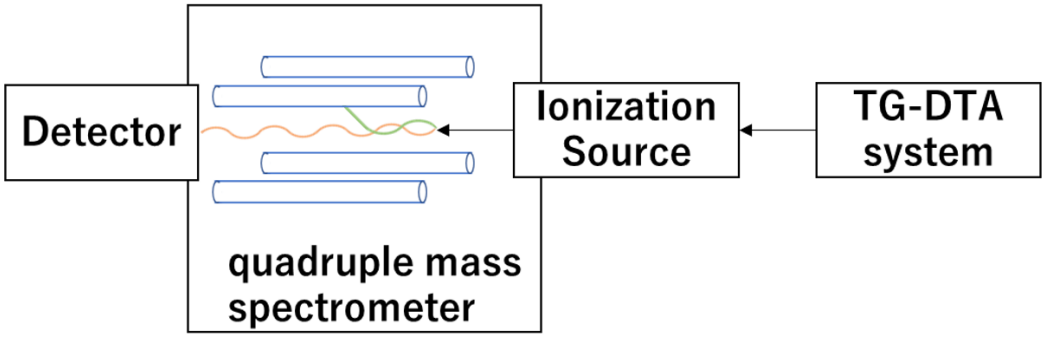

Figure 3.4.2 a schematic diagram of the MS system (the quadruple mass spectrometer)

the voltage, only ions of a specific mass reach the detector and their intensity is measured.

Procedure

As in procedure 3.2.2, ZrP absorbed ammonia (0.4, 1.6 and 2.0 mol(NH_3)mol^{-1}(ZrP)) was prepared by adding ZrP to various concentration of ammonia water, respectively. Then, all samples were dried vacuum overnight at room temperature. The thermal properties and gas desorption properties of all samples were investigated by TG-DTA apparatus (Rigaku, TG8120) and MS apparatus (Anelva, M-QA200TS). TG-DTA is installed inside the glove box to minimize an influence of exposing the samples to air and water (water level : below 0.2ppm), and MS apparatus connected to the TG-DTA equipment through a capillary. The pressure inside the MS spectrometer is less than 10^{-3} Pa due to the vacuum of a turbo molecular pump and rotary pump. In the TG-DTA-MS system, high purity Ar gas is flowed as a carrier gas.

About 10 mg of the samples was put into an Al pan and set to the balance in the TG-DTA apparatus. The heating rate was fixed to be 5 K min^{-1}.

3.5 Nuclear magnetic resonance (NMR) spectroscopy

Nuclear magnetic resonance (NMR) is a technique for analyzing molecular structures, inter/intramolecular interactions and molecular mobility of materials at an atomic level. A nucleus in an atom is composed of protons and neutrons. Due to the spin of protons and neutrons, the nucleus has a magnetic moment which is called a nuclear magnetic moment. According to the shell model, protons or neutrons form pairs of opposite angular momenta. Thus, if the number of protons and neutrons are even, the nuclear magnetic moment is zero and the spin quantum number (nuclear spin) of the nucleus is also zero. Table 3.5 shows number of protons and neutrons, spin quantum number and natural abundance for nuclei.

Table 3.5 The data of various nuclei [2,6]

Isotope	Number of proton	Number of Neutron	Spin quantum number I	Natural abundance (%)
^{1}H	1	0	1/2	99.985
^{2}H	1	1	1	0.015
^{12}C	6	6	0	98.92
^{13}C	6	7	1/2	1.08
^{14}N	7	7	1	99.63
^{15}N	7	8	1/2	0.037
^{16}O	8	8	0	99.74
^{17}O	8	9	5/2	0.037
^{18}O	8	10	0	0.205
^{27}Al	13	14	5/2	100
^{28}Si	14	15	0	92.22
^{29}Si	14	16	1/2	4.69
^{30}Si	14	17	0	3.09
^{31}P	15	16	1/2	100

The nucleus exhibit precessional motion in a magnetic field (Larmor precession). The precessional motion of the nucleus has a fixed period of rotation. By adding radio waves (60 MHz to 1 GHz) of the same frequency as the period of rotation, resonance occurs. At this time, the nucleus generates an electromagnetic signal.

The nucleus, with a spin quantum number other than zero, splits into 2I+1 energy levels in an external magnetic field (Zeeman effect). For example, in a nucleus with a nuclear spin quantum number of 1/2, the nuclear spin split into two spin states by a magnetic field. Originally, nuclear spins exist in a random. When a magnetic field is applied from outside, the nuclear spins are divided into a stable state (α-spin) with the same direction as the magnetic field and an unstable state (ß-spin) with the opposite direction (Figure 3.5.1).

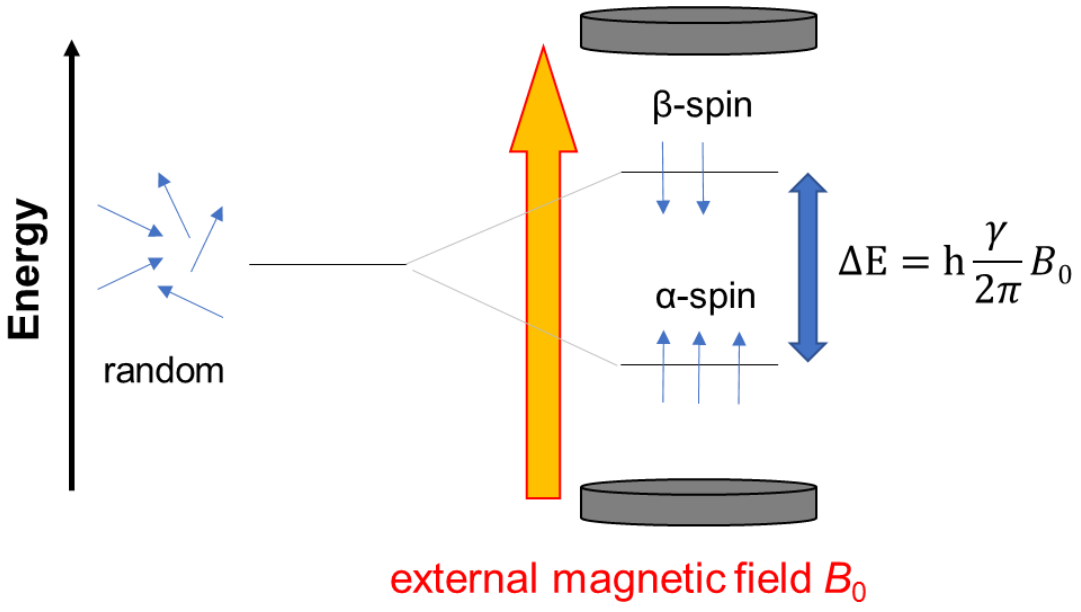

Figure 3.5.1 Energy level of nuclear spins due to external magnetic field [6]

The energy difference ΔE is proportional to the intensity B_0 of the applied external magnetic field and is expressed by the following equation.

$$\Delta E = \mathrm{h}\frac{\gamma}{2\pi}B_0 = hv \qquad \text{(Equation 3.5.1)}$$

where h is a Planck constant (6.62607015×10^{-34} J s), γ is called a gyromagnetic ratio and v is called a resonance frequency which is irradiated radio waves. γ is a value specific to the nucleus such as 2.675×10^{8} $T^{-1}s^{-1}$ for ^{1}H, 6.73×10^{7} $T^{-1}s^{-1}$ for ^{13}C, and 1.084×10^{8} $T^{-1}s^{-1}$ for ^{31}P. The nucleus in the α spin state is partially inverted to the β spin state when the radio wave is absorbed. The excited nucleus emits radio waves of the same frequency and returns to the α-spin state. The NMR spectroscopy detects the emitted radio waves and calculates and records the signal intensity by Fourier transform. In a molecule, the nucleus is surrounded by a cloud of electrons. The electrons produce a local magnetic field in response to a magnetic field. Therefore, the effective magnetic field received of the nucleus, is the difference between the external magnetic field and the local magnetic field induced by the external magnetic field. Such a phenomenon is called magnetic shielding.

Generally, NMR spectrum is analyzed by a chemical shift. Chemical shift is defined as a "relative changes in shielding caused by changes in the chemical environment". It is assumed that there are two nuclei with different shielding constants given by σ_1 and σ_2 due to the difference in the chemical environment, and these are placed in the magnetic field B_0. The

resonance frequencies ν_1 and ν_2 of these nuclei are given by the following equations.

$$\nu_1 = \frac{\gamma B_0}{2\pi}(1 - \sigma_1) \quad \text{(Equation 3.5.2)}$$

$$\nu_2 = \frac{\gamma B_0}{2\pi}(1 - \sigma_2) \quad \text{(Equation 3.5.3)}$$

Here, σ_1 and σ_2 is much smaller than 1. Therefore, the chemical shift (δ) is expressed by the following equation

$$\delta = \frac{\nu_1 - \nu_2}{\nu_1} \fallingdotseq \sigma_2 - \sigma_1 \quad \text{(Equation 3.5.4)}$$

The ratio of the change in frequency is equal to the difference in shielding due to the difference in environment between the two nuclei.

The spectra of solid samples have broadened line widths due to interactions between various nuclear spins and other factors. The cause of the broadening differs depending on the nuclide measured. The most common ways are the following: (i)the anisotropy of the chemical shift caused by the anisotropy of the electron distribution around the measuring nucleus (ii) the broadening of the linewidth due to the dipole-dipole interaction between the measured nucleus and nearby nuclei (especially ^{1}H). The following two methods are used to extract high-resolution spectra close to solution from such a wide range of solid spectra. MAS (Magic Angle Spinning) and ^{1}H high-power decoupling are the most common methods. In general, both are used.

In MAS, the sample is tilted at 54.4° (called magic angle) to the magnetic field and rotated at high speed (3-15 kHz). This allows the sample to be oriented in any direction relative to the magnetic field, which averages out the chemical shifts and results in a slightly sharper spectrum. However, when ^{1}H is present near the nucleus, it is not possible to achieve high enough resolution for structural analysis because of the broadening of the line due to the dipole-dipole interaction with the hydrogen nucleus. By irradiating the ^{1}H side of the nucleus with high-power radio waves using the ^{1}H high-power decoupling technique, the dipole-dipole interaction with the ^{1}H nucleus is averaged out and disappears, and a high-resolution spectrum close to that of the solution is obtained.

P is contained in functional materials such as layered phosphate and apatite, and it is important to determine the state of P in order to elucidate their functions. It is important to understand its function. Experimentally, ^{31}P is a very sensitive and easy to measure nucleus because of its 100% natural abundance. The nuclear spin is 1=1/2. The broadening of the line width is due to the anisotropy of the chemical shift and the dipole-monodipole interaction with the surrounding ^{1}H. Therefore, it is relatively easy to obtain high-resolution spectra by MAS method etc. 85% H_3PO_4 aqueous solution is used as a reference for the chemical shift.

Layered zirconium phosphate has both α-type and γ-type structures. The ^{31}P MAS NMR spectra of α-$Zr(HPO_4)_2$-H_2O and γ-$Zr(H_2PO_4)(PO_4)$-$2H_2O$ were reported. Three phosphate groups, $(HPO_4)^{2-}$, $(H_2PO_4)^{-}$, and $(PO_4)^{3-}$, were attributed to peaks at -18.7, -9.4, and -27.4 ppm, respectively.

Although limited to layered phosphates, the chemical shift values in Figure 3.5.1 show that we can easily attribute the three phosphate groups $(HPO_4)^{2-}$, $(H_2PO_4)^-$, and $(PO_4)^{3-}$ and distinguish between their structural types, i.e., α- and γ-types.

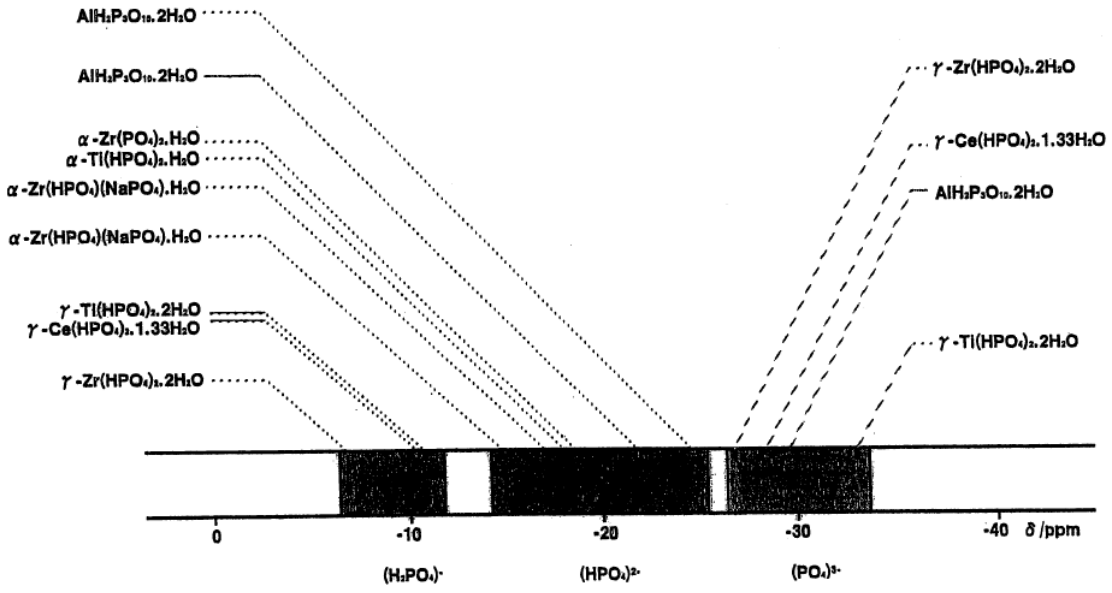

Figure 3.5.2 Chemical shift of layered phosphate in ^{31}P solid NMR [7]

Procedure

^{31}P MAS NMR measurements can provide information on the environment around the radionuclide due to chemical shifts depending on the electronic state of the radionuclide. ^{31}P was used to measure the nuclide. As in procedure 3.2.2, ZrP absorbed ammonia (0.4, 1.6 and 2.0 $mol(NH_3)mol^{-1}(ZrP)$) was prepared by adding ZrP to various concentration of ammonia water, respectively. ZrP and ZrP absorbed ammonia (0.4, 1.6 and 2.0 $mol(NH_3)mol^{-1}(ZrP)$) were dried vacuum overnight at room

temperature. After vacuum, all samples were handled in a glovebox purified by a gas recycling purification system to minimize influence of water in the air. The water level was kept below 0.1 ppm. Then, in the glovebox, the prepared samples were sealed in sample cells, respectively. Solid-state NMR measurements were performed with an ECA600 manufactured by JEOL Co. ltd. A chemical shift is defined as the difference in parts per million (ppm) between the resonance frequency of the observed ^{31}P and that of the Phosphoric acid ^{31}P.

3.6 Fourier transform infrared (FTIR) spectroscopy

Infrared (IR) spectroscopy is a technique for the evaluation of intramolecular interactions and quantitation. Infrared radiation is radio wave, with a wavelength longer than red light and shorter than radio waves of millimeter wavelengths. For typical IR spectroscopy, infrared radiation is mid-infrared radiation with wavelengths of about 2.5-25 μm (about 4000-400 cm^{-1} in wavenumber).

When radio waves are irradiated on a molecule and the Bohr's quantum condition is satisfied, a part of the radio wave energy is transferred to the molecule. The molecule absorbs the energy difference between the two quantum states by transitioning from the ground state to the excited state. Here, the kinetic energy of the molecule is classified into three categories: vibrational energy, rotational energy and translational energy. The energy of infrared radiation is closed to vibrational energy, and thus the molecules absorbed the infrared radiations. Since the wavelength and intensity of absorption are specific to the type of atom and bonding mode, the type of chemical bonding is determined by analyzing the amount of absorption at each energy (wavenumber).

The bonds between two atoms have spring-like properties as shown in Figure 3.6.1. The frequency of vibration v_{fv} between the two atoms is expressed by the following equation,

$$v_{fv} = \frac{1}{2\pi}\sqrt{\frac{k}{M}} \qquad \text{(Equation 3.6.1)}$$

$$M = \frac{m_1 m_2}{m_1 + m_2} \qquad \text{(Equation 3.6.2)}$$

where m_1 and m_2 are the masses of two atoms, and k is spring constant. Infrared radiation of the wavelength as this frequency is absorbed by molecular vibrations. The exception is when the vibration of the molecule is not accompanied by a change in dipole moment. A dipole is a charge distortion caused by the bias of electrons in a molecule and a dipole moment represents a quantity that expresses the strength of a dipole that indicates a pair of positive and negative charges of equal size separated by a small distance.

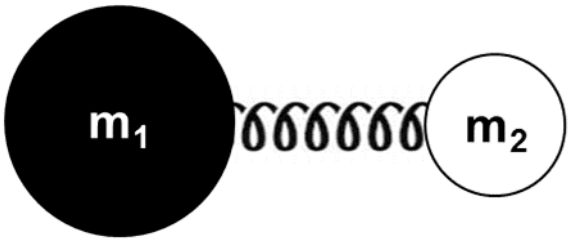

Figure 3.6.1 The model of molecule composed of two atoms [6]

In the case of CO_2 (linear molecule), symmetric stretching vibrations do not absorb infrared light because the dipole moment does not change, but antisymmetric stretching vibrations do absorb infrared light because the dipole moment changes. The infrared is not absorbed for the diatomic molecules such as H_2, O_2 and N_2 because the dipole moment is not changed even if the vibration is happened. These are examples of infrared absorption due to stretching vibrations. Furthermore, infrared absorption can also be

observed in angular and rotational vibrations when accompanied by a change in the dipole moment.

Figure 3.6.2 shows the FTIR spectra of ammonia gas. 50 mmHg (NH_3) diluted to a total pressure 600 mmHg with N_2. The infrared absorption of N-H shows three peaks. The peak from 3500 to 3200 cm^{-1} is a stretching vibration of N-H. The peak from 1700 to 1500 cm^{-1} is a bending vibration of N-H.

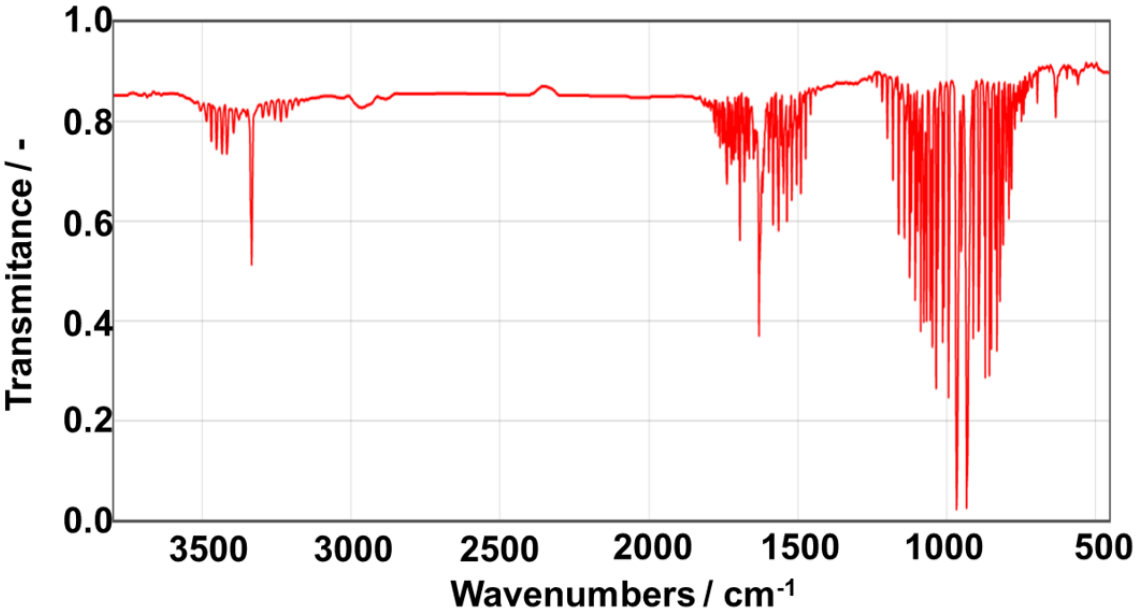

Figure 3.6.2 FTIR spectrum of NH_3 gas (50 mmHg(NH_3) / 600 mmHg(total)) [8]

Figure 3.6.3 shows the FTIR spectra of NH_4HSO_4 and $(NH_4)_2SO_4$. The infrared absorption of N-H shows three peaks. The peak from 3300 to 3000 cm^{-1} is a stretching vibration of N-H. The peak under 1500 cm^{-1} is a bending vibration of N-H from NH_4^+.

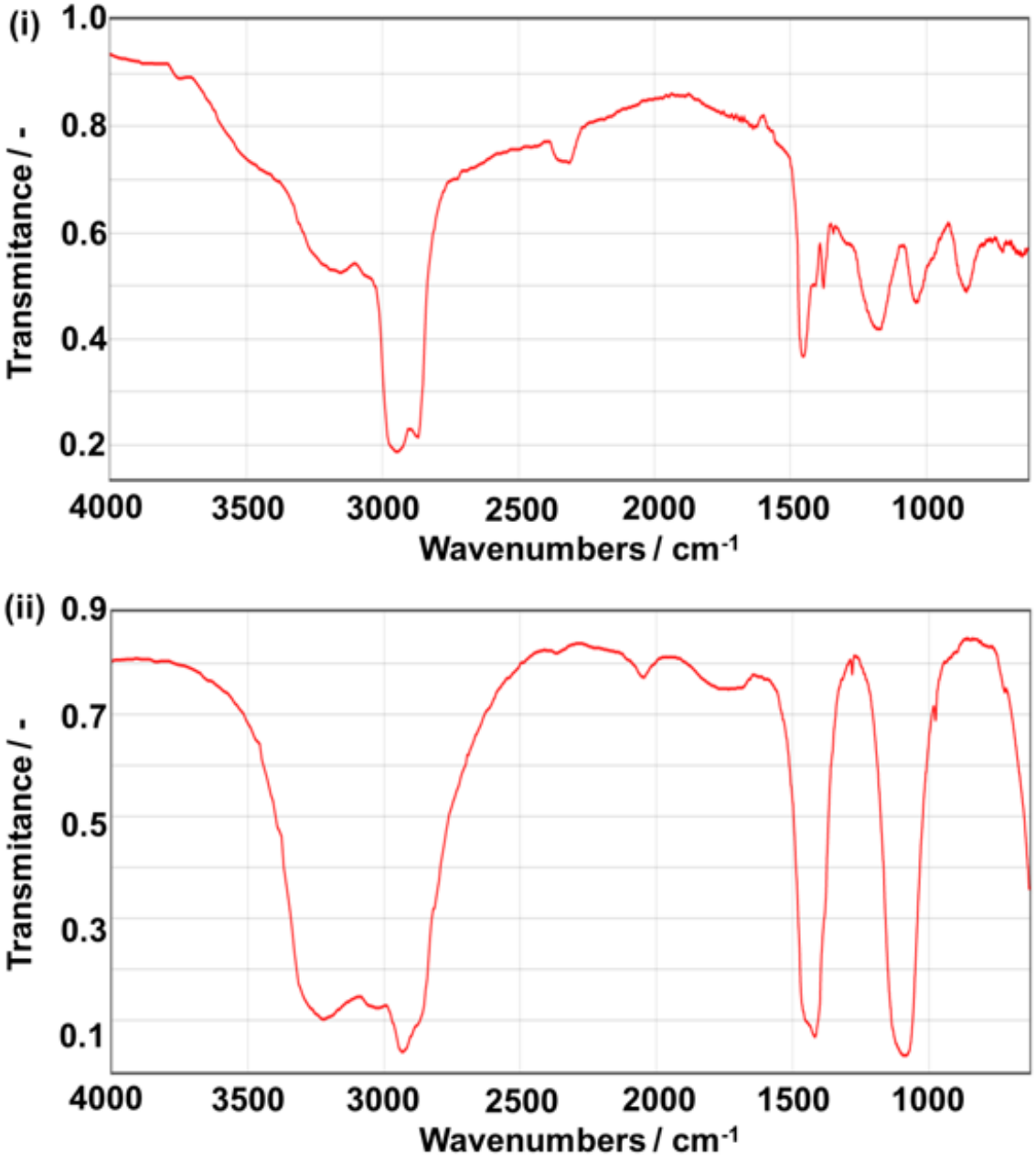

Figure 3.6.3 FTIR spectrum of (i)NH_4HSO_4 and (ii) $(NH_4)_2SO_4$. [9,10]

Table 3.6 Characteristic IR absorption band [6]

Group	cm^{-1}	Shape (strength)
$-NH_4^+$	3300-3030 1430-1390	Broad , (Strong) Strong

The characteristic IR absorption band position changes with structural factors such as electrical effects and steric effects.

Procedure

FTIR system (spectrum one manufactured by Perkin Elmer Co., Ltd) equipped with diffuse reflection cell were used to observe infrared absorption spectra. As in procedure 3.2.2, ZrP absorbed ammonia (0.4, 1.6 and 2.0 mol(NH_3)mol^{-1}(ZrP)) was prepared by adding ZrP to various concentration of ammonia water, respectively. Then, all samples were dried vacuum overnight at room temperature. After vacuum, all samples were diluted to 1 wt.% in the KBr powder in a glovebox purified by a gas recycling purification system (MP-P60W manufactured by Miwa MFG Co., Ltd.) to minimize influence of water in the air. The water level was kept below 0.1 ppm. The prepared samples were placed in a sample cell under argon atmosphere. The background measurement was performed using a KBr pellet in the cell. The data were recorded and averaged 10 times with a spectral resolution of 4 cm^{-1} in the range of 4000-500 cm^{-1}.

3.7 Ammonia removal system of water and solid material

Experimental study was conducted to remove ammonia from simulated leaked ammonia gas using a new system that mixes water and solid acid. Thus, it is essential to measure ammonia gas concentration. The most popular method of ammonia gas concentration measurement is to use a Kitagawa-type gas detector. The Kitagawa-type gas detector consists of a detector tube and a gas sampler. When the detector tube is filled with a sample gas, the chemical reacts with the specific gas and changes color. The length of the discoloration is proportional to the gas concentration. Therefore, the gas concentration can be determined simply by reading the scale on the discolored tip. In the case of ammonia detector tube, the tube contains phosphoric acid and an indicator that changes color depending on pH. When phosphoric acid and ammonia react, the pH changes and then the color of the indicator changes.

Procedure

Figure 3.7 shows a vessel for the simulated leaked ammonia gas removal experiment. 1 g of α-ZrP was dispersed in 30 g of water. N_2 gas (100,000 Pa) containing 1010 ppm (101 Pa) of ammonia was prepared by Taiyo Nippon Sanso and was used as a simulated leaked ammonia gas. The vessel with an internal volume of 32 L was vacuumed, and then simulated leaked ammonia gas was introduced in the vessel up to 0.1 MPa at 293 K. The amount of ammonia in the vessel was 1.33 mmol, which was calculated using the equation of state for ideal gas. A fan is set up in the vessel for the

uniform concentration. The change in ammonia concentration was measured after aqueous dispersion of ZrP or water was fed through a hole at the top of the vessel. A Kitagawa-type gas sampler and three types of detector tubes (105SM: NH_3 0.1-1%, 105SB: NH_3 50-900 ppm, and 105SD: NH_3 0.2-20 ppm) were used to measure ammonia concentrations in the gas.

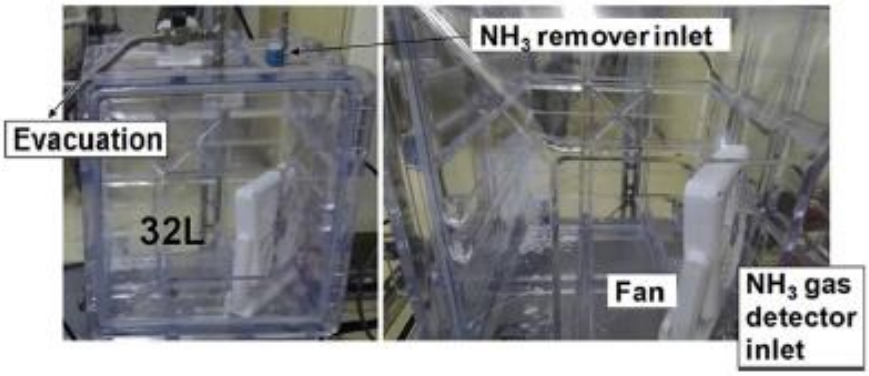

Figure 3.7 Overview of a vessel for simulated leaked ammonia gas at 1010 ppm [11].

References

[1] K. Motokura, Y. Iwasawa, *The Clay Science Society of Japan*, **48** (2009) 58-63.

[2] *Shriver and Atkins' Inorganic chemistry, 5th revised edn.*, P. Atkins, T. Overton, J. Rourke, M. Weller, and F. Armstrong, Oxford University Press., 2009.

[3] National Effluent Standards, Retrieved December 29th, 2020 from https://www.env.go.jp/en/water/wq/nes.html

[4] Henry's Law constant (water solution) of ammonia, Retrieved December 29th, 2020 from https://webbook.nist.gov/cgi/cbook.cgi?ID=C7664417&Units=SI&Mask=10#Solubility

[5] *X-ray Structure Analysis*, *3th edition,* K. Waseda, and E. Matubara, Uchida Rokakuho Publishing Co. Ltd, 2002, Japan.

[6] *Spectrometric Identification of Organic Compounds*, *8th edition*, R.M. Silverstein, F.X. Webster, D.J. Kiemle, Wiley, 2012.

[7] H. Nakayama, T. Eguchi, N. Nakamura, S. Yamaguchi, M. Danjyo, and M. Tsuhako, *J. Mater. Chem.*, **6** (1997) 1063-1066.

[8] IR spectrum of Ammonia, Retrieved December 29th, 2020 from https://webbook.nist.gov/cgi/cbook.cgi?ID=C7664417&Units=SI&Type=IR-SPEC&Index=1#IR-SPEC

[9] IR spectrum of Ammonium bisulfate, Retrieved December 29th, 2020 from https://webbook.nist.gov/cgi/cbook.cgi?ID=C7803636&Units=SI&Mask=80#IR-Spec

[10] IR spectrum of Ammonium sulfate, Retrieved December 29th, 2020 from https://webbook.nist.gov/cgi/cbook.cgi?ID=C7783202&Units=SI&Type=IR-SPEC&Index=1#IR-SPEC

[11] M. Yamaguchi, T. Ichikawa, H. Miyaoka, T. Zhang, H. Miyaoka, Y. Kojima, *Int J. Hydrogen Energy*, **45** (2020) 22189-22194.

4. Results and Discussion

4.1 A new concept of ammonia removal system combined water and an insoluble proton-based solid acid

Water, similarly to ammonia, is a polar substance and has hydrogen bonding. Thus, the solubility and diffusion coefficient of ammonia in water are large and water easily collects gaseous ammonia [1]. However, the ammonia equilibrium vapor pressure of water is proportional to the ammonia concentration (ammonia storage capacity) in ammonia water [2,3]. Therefore, an ammonia storage material mixed with water would be possible to make an ammonia removal system that has the absorption rate of water and the low ammonia concentration.

Metal halides such as $MgCl_2$ form metal ammine complex salts with low ammonia vapor pressure. Moreover, $CuSO_4$ forms metal ammine complex salt with low ammonia vapor pressure below 0.2 Pa. However, these materials are soluble in water (Solubility at 298 K, $MgCl_2$: 56.0 g/ 100g(H_2O), $CuSO_4$: 22.4 g/100g(H_2O)) [4,5].

Complex hydrides form metal borohydride ammine complex salts with ammonia vapor pressure above 30 Pa. Although these materials react with water to generate hydrogen and metal hydroxide [6-8]. To make the solution basic, it facilitates the release of ammonia from ammonia water.

Proton-based materials form ammonium ion with low ammonia vapor pressure below 0.2 Pa [5, 9-12]. These materials are classified into soluble and insoluble materials in water. NH_4HSO_4 reacts with NH_3 to form $(NH_4)_2SO_4$ and is soluble in water (solubility at 298 K, $(NH_4)_2SO_4$: 76.4 g/

100g(H_2O)). The soluble proton-based materials only convert NH_3 into NH_4^+ and cannot reduce nitrogen concentration in the solution. To reduce the negative environmental effects, insoluble ammonia storage materials are required that reduce the ammonia concentration in gas and water.

Insoluble proton-based materials such as proton-based solid acids absorb NH_3 and the equilibrium pressure is below 0.2 Pa. Thus, insoluble proton-based solid acids will be used to remove nitrogen from ammonia water. α-zirconium phosphate [10], acid-impregnated charcoal [9,13], proton exchanged zeolite [14] and proton-exchanged montmorillonite [15, 16] will be candidates as insoluble proton-based solid acids. Therefore, a new system combined water and insoluble proton-based solid acids will absorb gaseous ammonia to low ammonia pressures.

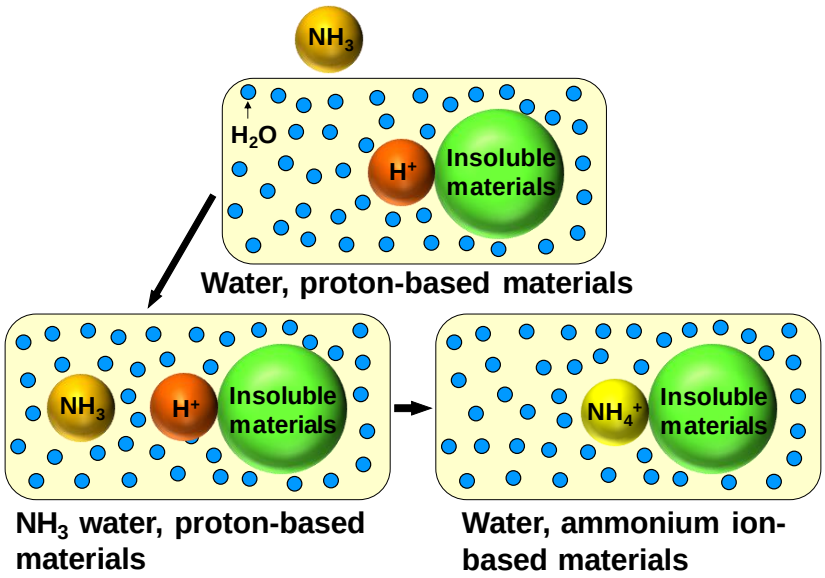

Figure 4.1 A conceptive picture of an ammonia removal system combined water and proton-based materials [17].

4.2 Insoluble proton-based solid acids for ammonia ad/absorption

4.2.1 Ammonia ad/absorption of proton-based solid acids in water

Figure 4.2.1(i) shows the time variation of NH_3 and H^+ concentration in ammonia water when ZrP is added. The NH_4^+ concentration calculated from the equation 3.2.1 is also indicated. The NH_3 concentration decreased and the pH increased with time. As a result, the NH_4^+ concentration was almost constant.

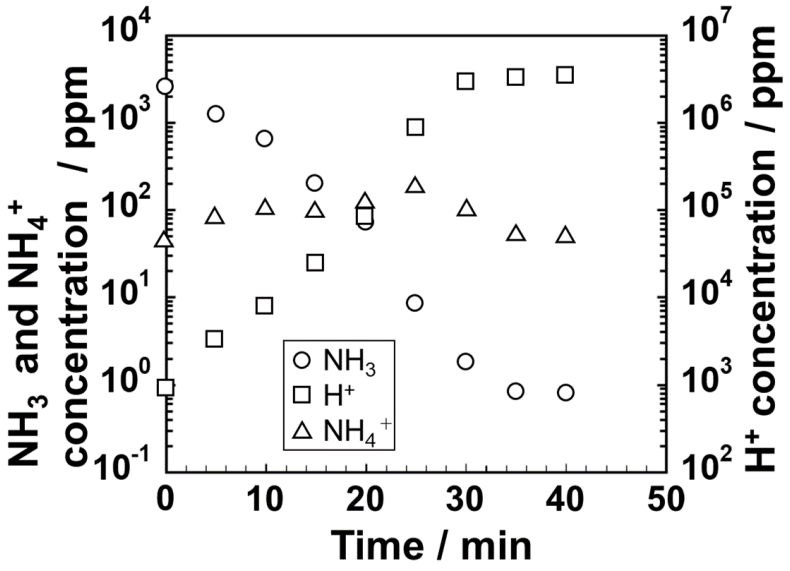

Figure 4.2.1 NH_3, H^+ and NH_4^+ concentrations in ammonia water as a function of time

The nitrogen concentration in the solution is calculated from the NH_3 and NH_4^+ concentrations using the following equation 3.2.3. Figure 4.2.2(i) shows the time variation of nitrogen concentration in ammonia water when each sample is added. The nitrogen concentration in the solution dropped from about 2000 ppm to lower than about 100 ppm, in about 30 minutes with the addition of α-zirconium phosphate. Therefore, it is useful to

suppress the water pollution.

Ammonia storage capacity is calculated from the nitrogen concentration using the following equation 3.2.2. Figure 4.2.2 (ii) shows the ammonia ad/absorption profiles of zirconium phosphate, zeolite and $CaHPO_4 \cdot 2H_2O$ for reaction with ammonia water carried out at 293-298 K. $CaHPO_4 \cdot 2H_2O$ does not absorb ammonia in the solution. $MgHPO_4 \cdot 3H_2O$ also absorbs little ammonia and shows a similar profile to $CaHPO_4 \cdot 2H_2O$. It has been reported that ammonia storage capacities of bamboo charcoal and

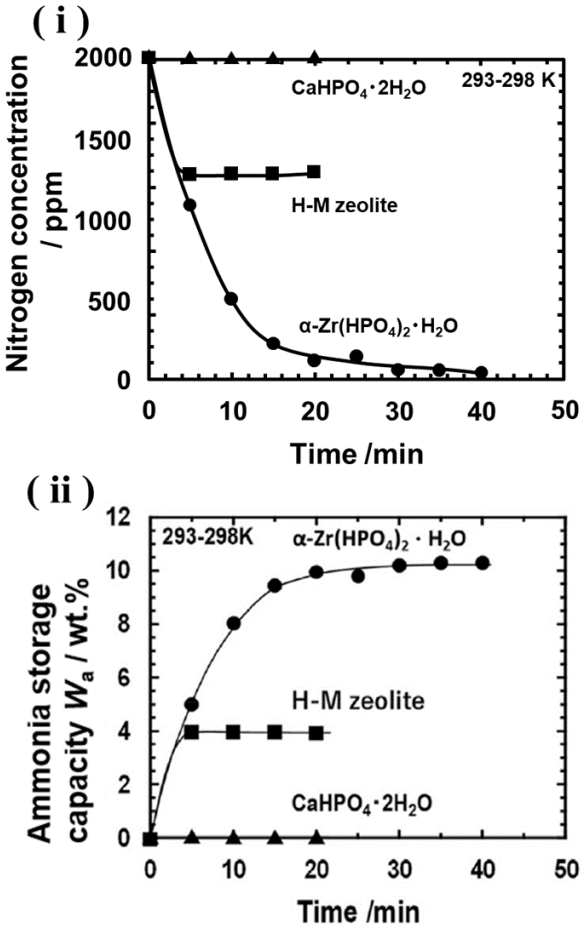

Figure 4.2.2 (i) nitrogen concentrations in ammonia water as a function of time (ii) ammonia ad/absorption profiles for reaction of proton-based solid acids and $CaHPO_4 \cdot 2H_2O$ with ammonia water [19].

activated carbon with acid treatment were below 1 wt% in ammonia water [18]. Then, H-M zeolite absorbs ammonia and the adsorption capacity is 4.0 wt%. The other porous materials (H-mont, Impregnated AC and H-Y zeolite), as well as H-M zeolite, reach constant storage capacities after about 5-10 minutes, respectively. It was found that ZrP slowly absorbs ammonia and has large capacity of 10.2 wt%. The ammonia storage capacity of ZrP has an error of ±0.5 wt%.

Table 4.2 shows the ammonia storage capacities from the solutions for proton-based solids acids, $Ca(HPO_4)\cdot 2H_2O$ and $Mg(HPO_4)\cdot 3H_2O$. Among these samples, ZrP shows the maximum ammonia storage capacity. $Ca(HPO_4)\cdot 2H_2O$ and $Mg(HPO_4)\cdot 3H_2O$ also have H in those structures, but does not work as proton, thus ammonia is not absorbed.

Table 4.2 Ammonia storage capacity using different proton-based solid acids, $Ca(HPO_4)\cdot 2H_2O$ and $Mg(HPO_4)\cdot 3H_2O$ at 293-298 K [19].

Proton-based solid acids, $CaHPO_4\cdot 2H_2O$ and $MgHPO_4\cdot 3H_2O$	Ammonia storage capacity / wt%
Calcium hydrogen phosphate dihydrate $CaHPO_4\cdot 2H_2O$	0.00
Magnesium hydrogen phosphate trihydrate $MgHPO_4\cdot 3H_2O$	0.08
Proton exchanged montmorillonite H-mont	1.65
Impregnated activated carbon Impregnated AC	2.12
Proton exchanged Y type zeolite H-Y zeolite	2.46
Proton exchanged mordenite type zeolite H-M zeolite	3.98
α-zirconium phosphate (ZrP) $\alpha\text{-}Zr(HPO_4)_2\cdot H_2O$	10.2

4.2.2 The relation between ammonia storage capacity and proton exchange capacity of proton-based solid acids

Proton-based solid acids (H-mont, H-Y zeolite, H-M zeolite, α-$Zr(HPO_4)_2 \cdot H_2O$) are considered to react with ammonia to form ammonium ions. Figure 4.2.3 shows the relation between ammonia storage capacities (W_a) and the proton exchange capacities (P_{ec}) of these samples. Calculated line was obtained by the following equation.

$$W_a = \frac{0.01703P_{ec}}{1 + 0.01703P_{ec}} \times 100 \qquad \text{(Equation 4.2)}$$

The ammonia storage capacity and theoretical proton exchange capacity of Proton-based solid acids correspond to the calculated values. Therefore, the reaction is considered to be by proton exchange.

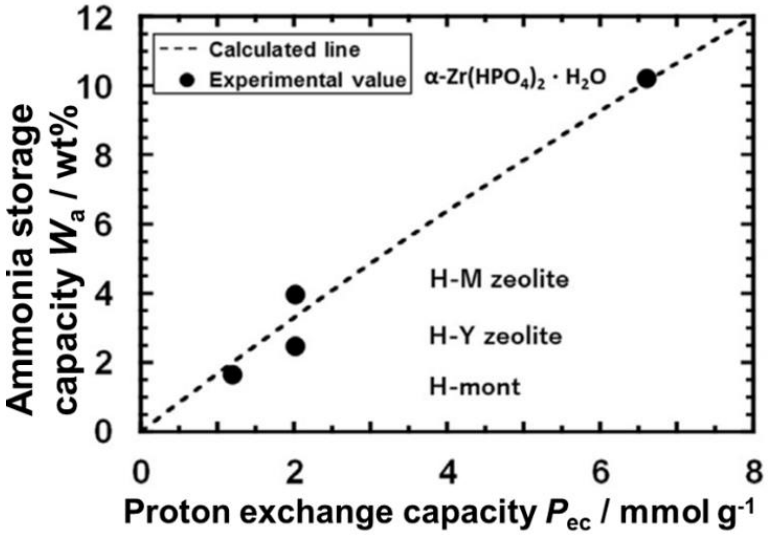

Figure 4.2.3. Relation between ammonia storage capacities and proton exchange capacities [19].

4.3 Thermodynamics of a layered solid acid (ZrP) absorbed ammonia

4.3.1 Ammonia concentration composition isotherm of ZrP

Figure 4.3.1 shows the ammonia concentration composition isotherm (CCI) of α-$Zr(HPO_4)_2 \cdot H_2O$ (ZrP). The NH_3 equilibrium concentration is lower than 0.01 ppm below the ammonia storage capacity (ammonia storage capacity) about 3 mmol g^{-1} (1 mol(NH_3)mol^{-1}(ZrP)). ZrP has the NH_3 equilibrium plateau concentration of ca. 1 ppm in the range of ammonia storage capacity from 4 to 6 mmol g^{-1} (1 to 2 mol(NH_3)mol^{-1}(ZrP)). Therefore, it is suggested that the two phases coexist in that range of ammonia storage capacity. The increase in the equilibrium concentration of ammonia from 3 to 4 mmol g^{-1} will be based on the appearance of $Zr(NH_4PO_4)_2 \cdot H_2O$ phase. Subsequently, when ZrP absorbed ammonia above 6 mmol g^{-1} (2 mol(NH_3)mol^{-1}(ZrP)), the NH_3 equilibrium concentration drastically increases. This capacity corresponds to the proton exchange capacity of ZrP (6.6 mmol g^{-1}). It is suggested that ammonia is bonded to the proton of ZrP and form ammonium ion below 6 mmol g^{-1} (2 mol(NH_3)mol^{-1}(ZrP)). The NH_3 equilibrium concentration also increases above 6 mmol g^{-1} (2 mol(NH_3)mol^{-1}(ZrP)) because all the protons of ZrP reacted with ammonia. According to ammonia CCI, we can interpret that two kinds of ammonia absorption sites exist in ZrP, which is shown in the formula,

$$Zr(HPO_4)_2 \cdot H_2O + NH_3 \rightleftharpoons Zr(NH_4PO_4)(HPO_4) \cdot H_2O \qquad \text{(Equation 4.3.1)}$$

$$Zr(NH_4PO_4)(HPO_4) \cdot H_2O + NH_3 \rightleftharpoons Zr(NH_4PO_4)_2 \cdot H_2O \qquad \text{(Equation 4.3.2)}$$

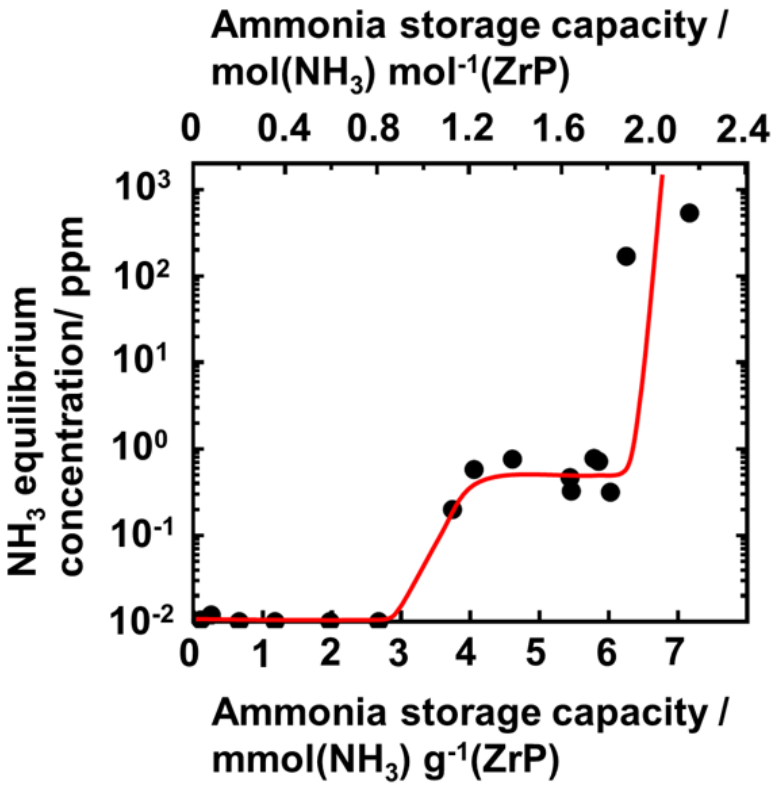

Figure 4.3.1. Ammonia CCI plots in water of ZrP at about 298 K [20].

Figure 4.3.2 shows ammonia CCI of the H-Y zeolite as a reference. Below the ammonia storage capacity of 0.7 mmol g^{-1}, the NH_3 equilibrium concentration is below the detection limit (0.01 ppm). When storing ammonia above this value, the ammonia concentration increases with the storage capacity. For example, with the ammonia storage capacity of 2 mmol g^{-1} (equivalent to the proton exchange capacity), the ammonia concentration reaches about 500 ppm. This ammonia CCI profile is considered to be due to the porous structure of the H-Y zeolite and the fact that structural phase change does not occur during ammonia adsorption.

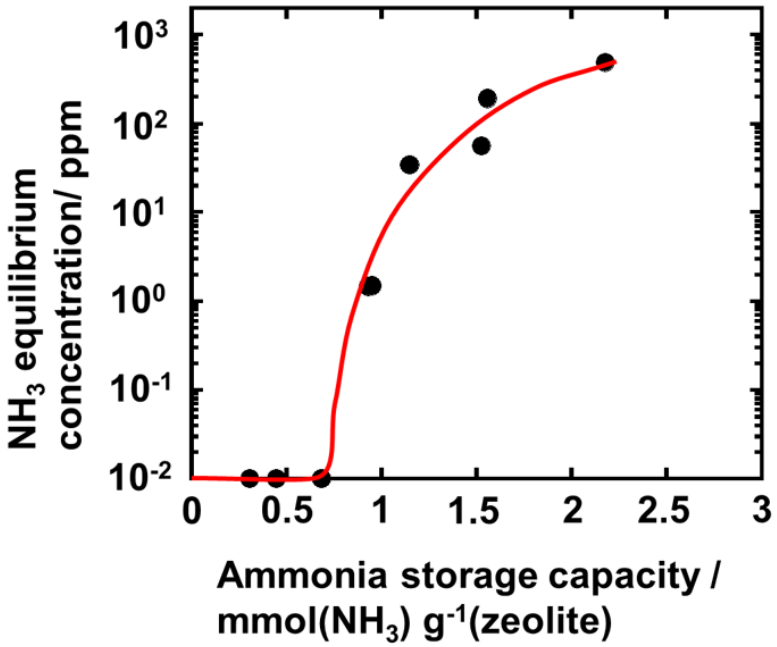

Figure 4.3.2. Ammonia CCI plots in water of proton exchanged Y type zeolite (H-Y zeolite) at about 298 K [20].

4.3.2 Ammonia concentration composition temperature of ZrP

Figure 4.3.3 shows the ammonia concentration composition temperature (CCT) curves of ZrP at 277 K and 313 K. At 313 K, the equilibrium plateau concentration around 0.1 ppm is observed in the range of ammonia storage capacity from 0 to 0.5 mol(NH_3)mol^{-1}(ZrP). Therefore, it is suggested that the two phases coexistence in this plateau region. The equilibrium concentration of 1 ppm at 0.8 mol(NH_3)mol^{-1}(ZrP) for ammonia absorption in ZrP is probably based on the appearance of $Zr(NH_4PO_4)_2 \cdot H_2O$. The equilibrium plateau concentration was observed in the range of ammonia storage capacity from 1 to 2 mol(NH_3)mol^{-1}(ZrP). The equilibrium plateau concentration in the range of ammonia storage capacity from 1 to 2 mol(NH_3)mol^{-1}(ZrP) increase with the temperature.

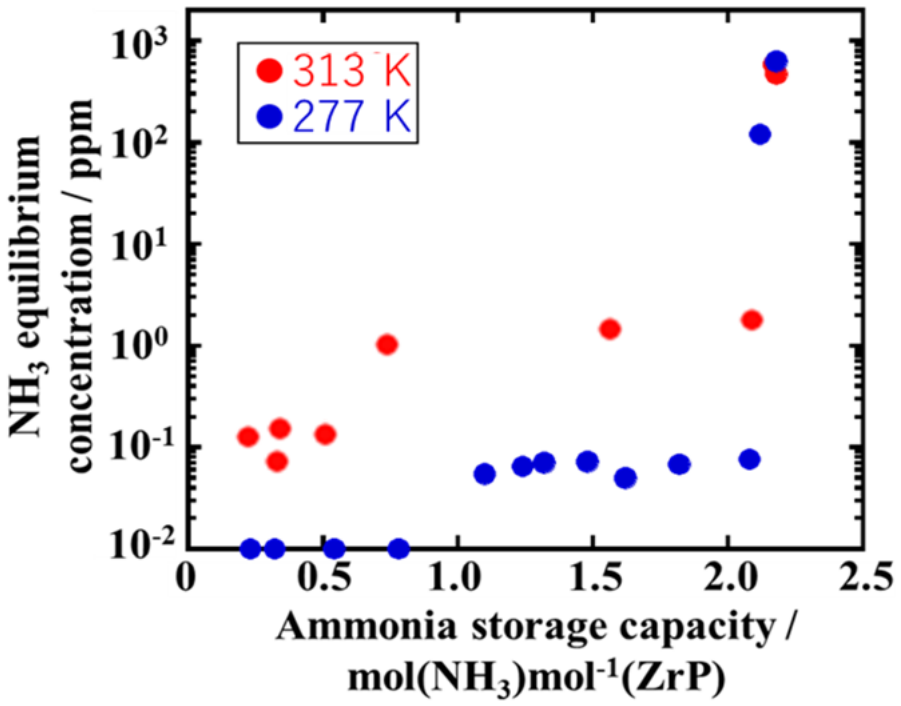

Figure 4.3.3 ammonia CCI plots of ammonia absorption for the ZrP at ca. 277 K and 313 K.

4.3.3 van't Hoff plot of ZrP absorbed ammonia

The relation between natural logarithm of mole fraction of ammonia ln c and inverse of the temperature 1/T is called the van't Hoff plot. In this thesis, the NH_3 equilibrium concentration is measured in unit of ppm. Therefore, the mole fraction of ammonia was calculated from the NH_3 equilibrium concentration C_{eq} using the following equation,

$$c_m = \frac{C_{eq} \times M_{H2O}}{\rho_{H2O} \times M_{NH3}} \times 10^{-6} \qquad \text{(Equation 4.3.3)}$$

where M_{H2O} and M_{NH3} are molar mass of H_2O and NH_3, respectively. ρ_{H2O} is density of water at several temperature.

Figure 4.3.4 shows the van't Hoff plot of ammonia CCT in the reaction equation 4.3.2. ΔH_w^0 is -64 kJ $mol^{-1}(NH_3)$ and ΔS_w^0 is -96 J K^{-1} $mol^{-1}(NH_3)$.

For equation 3.2.6, the ΔH^0 and ΔS^0 of ZrP absorbed ammonia [$Zr(NH_4PO_4)(HPO_4)\cdot H_2O + NH_3 \rightleftharpoons Zr(NH_4PO_4)_2\cdot H_2O$] are -95 kJ $mol^{-1}(NH_3)$ and -200 J $K^{-1}mol^{-1}(NH_3)$, respectively. These values are similar to the ΔH^0 and ΔS^0 of ammonium bisulfate absorbed ammonia [$NH_4HSO_4 + NH_3 \rightleftharpoons (NH_4)_2SO_4$] ($\Delta H^0$: -109 kJ $mol^{-1}(NH_3)$, ΔS^0: -191 J $K^{-1}mol^{-1}(NH_3)$) [21].

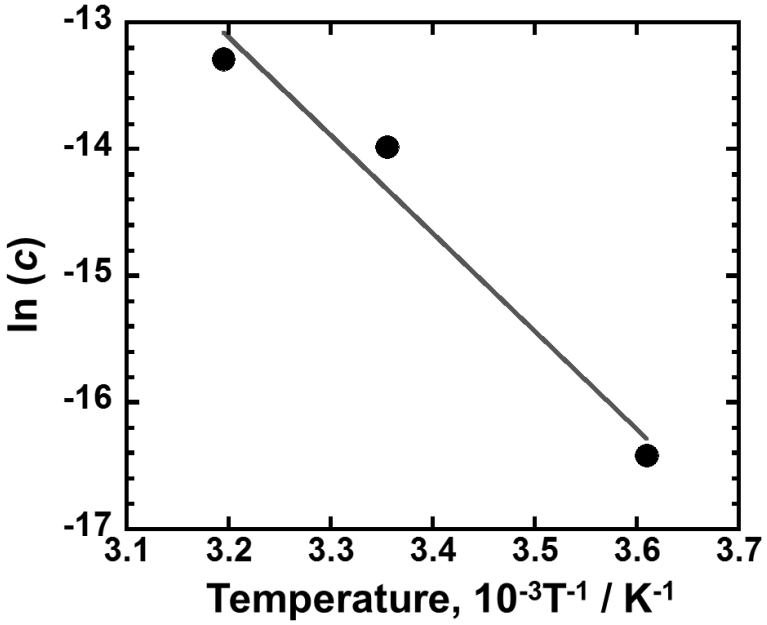

Figure 4.3.4 The van't Hoff plots of ZrP in the range 1-2 mol(NH_3)mol^{-1}(ZrP) on the equilibrium concentration as a function of the inverse of each experimental temperature (277 K, 298 K and 313 K) for the absorption.

Table 4.3 NH_3 equilibrium plateau concentration at 277, 298, 313K, standard enthalpy and entropy changes of ZrP absorbed ammonia

ZrP-absorbed ammona (mol(NH_3)mol^{-1}(ZrP))	NH_3 equilibrium plateau concentration / ppm			ΔH^0 / kJ $mol^{-1}(H_2)$	ΔS^0 / J K^{-1} $mol^{-1}(H_2)$
	277 K	298 K	313 K		
ZrP(0-1)	≤ 0.01	≤ 0.01	0.1	-	-
ZrP(1-2)	0.07	0.8	1.6	95	200

4.3.4 TG-DTA-MS spectra of ZrP absorbed ammonia

Fig. 4.3.5(i)(ii) show the temperature dependences of mass spectra with m/z 16 and 18 for $Zr(NH_4PO_4)_2 \cdot H_2O$ and $Zr(HPO_4)_2 \cdot H_2O$. Here, the signal of m/z 18 mainly refers to water (H_2O) and the signal of m/z 17 mainly refers to ammonia (NH_3). However, ammonia is defined as m/z 16 due to the water fragment ion (OH^-) effect on m/z 17. Fig. 4.3.5(i) shows the three peaks of m/z 16 for $Zr(NH_4PO_4)_2 \cdot H_2O$ around 390 K, 440 K and 610 K. It is indicated that $Zr(NH_4PO_4)_2 \cdot H_2O$ desorbs ammonia around these temperatures. Then, each peak of m/z 16 is compared by peak area, which correlates with the amount of ammonia desorption. The peak area of ammonia based on m/z 16 from 350 to 460 K is the same as the peak area of ammonia from 550 to 650 K. Thus, $Zr(NH_4PO_4)_2 \cdot H_2O$ is suggested to release ammonia in two steps, releasing 1 mol of ammonia from 350 to 460 K and 1 mol of ammonia from 550 to 650 K, respectively. The water desorption peaks of m/z 18 for $Zr(NH_4PO_4)_2 \cdot H_2O$ and $Zr(HPO_4)_2 \cdot H_2O$ are observed around 390 K and 410 K, respectively. The peak shift toward lower temperature of $Zr(NH_4PO_4)_2 \cdot H_2O$ may be based on the interaction between water and ammonia. Figure 4.3.5(iii)(iv) show the TG curves of $Zr(NH_4PO_4)_2 \cdot H_2O$ and $Zr(HPO_4)_2 \cdot H_2O$. In Figure 4.3.5(iii), two main weight losses are observed in this process. The weight loss of $Zr(NH_4PO_4)_2 \cdot H_2O$ from 330 to 460 K is 10.5 wt% and the weight loss from 550 to 650 K is 5.1 wt%. These weight losses are due to the desorption of ammonia and water. In Figure 4.3.6(iv), the weight loss of $Zr(HPO_4)_2 \cdot H_2O$ is 6.0 wt% from 330 to 460 K. Thus, $Zr(NH_4PO_4)_2 \cdot H_2O$ desorbs 1 mol water and 1 mol ammonia from 330 to 460

K, and desorbs 1 mol ammonia from 550 to 650 K by TG-MS measurement. Therefore, two kinds of ammonia absorption sites can exist in $Zr(NH_4PO_4)_2 \cdot H_2O$, as shown in the formula,

$$Zr(HPO_4)_2 \cdot H_2O \rightarrow Zr(NH_4PO_4)(HPO_4)+H_2O+NH_3 \quad \text{(Equation 4.3.4)}$$

$$Zr(NH_4PO_4)(HPO_4) \rightarrow Zr(NH_4PO_4)_2+NH_3 \quad \text{(Equation 4.3.5)}$$

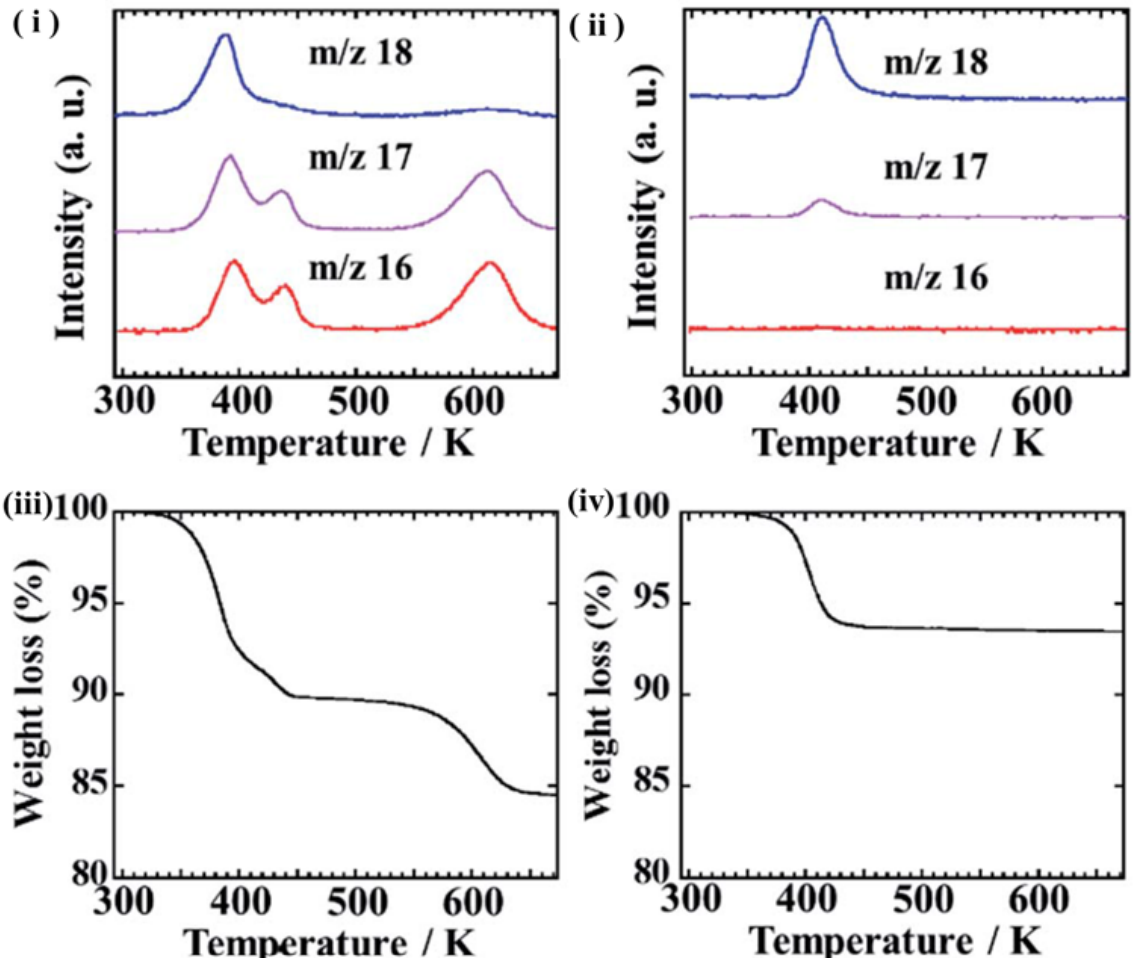

Figure 4.3.5 MS spectra of (i) $Zr(NH_4PO_4)_2 \cdot H_2O$ and (ii) $Zr(HPO_4)_2 \cdot H_2O$. Blue, purple and red lines are m/z 18, 17 and 16 curves. TG spectra of (iii) $Zr(NH_4PO_4)_2 \cdot H_2O$ and (iv) $Zr(HPO_4)_2 \cdot H_2O$ [20].

4.4. Fine structure of ZrP absorbed ammonia

4.4.1 pXRD patterns of ZrP absorbed ammonia

It has been reported that the $Zr(HPO_4)_2 \cdot H_2O$ and $Zr(NH_4PO_4)_2 \cdot H_2O$ has two-dimensional crystals [22,23]. $Zr(HPO_4)_2 \cdot H_2O$ and $Zr(NH_4PO_4)_2 \cdot H_2O$ have the interlayer distance of 0.76 nm and 0.96 nm, respectively. Figure 4.4.1 shows XRD patterns of ZrP, ZrP absorbed ammonia, $Zr(HPO4)_2 \cdot H_2O$ (JCPDS 00-019-1489) and $Zr(NH_4PO4)_2 \cdot H_2O$ (JCPDS 01-071-1633) of the International Center for Diffraction Data (ICDD). Figure 4.4.1(i) shows the small angle XRD patterns of ZrP and ZrP absorbed ammonia at 0.2 and 0.6 $mol(NH_3)mol^{-1}(ZrP)$. Only one peak around 2θ of 11.6 ° is observed for ZrP and ZrP absorbed ammonia(0.2 and 0.6 $mol(NH_3)mol^{-1}(ZrP)$). However, Figure 4.4.1(iii) shows new peaks around 24.5 and 33.3 °of ZrP absorbed ammonia (0.2 and 0.6 $mol(NH_3)mol^{-1}(ZrP)$), not present in ZrP and $Zr(NH_4PO_4)_2 \cdot H_2O$. According to figure 4.3.1, 4.3.3 and 4.3.6 of ZrP absorbed ammonia and the equation 4.3.1, the new peaks around 24.5 and 33.3 ° may come from the structure of $Zr(NH_4PO_4)(HPO_4) \cdot H_2O$. One possible explanation is that two phases observed by ammonia CCI are $Zr(HPO_4)_2 \cdot H_2O$ and $Zr(NH_4PO_4)(HPO_4) \cdot H_2O$ in the range of ammonia storage capacity from 0 to 1 $mol(NH_3)mol^{-1}(ZrP)$. Two peaks are observed for ZrP absorbed ammonia at 1.4 and 1.8 $mol(NH_3)mol^{-1}(ZrP)$ as shown in Fig. 4.4.1(ii). The peak around 2θ of 9.4 ° is the same as (0 0 2) diffraction of $Zr(NH_4PO_4)_2 \cdot H_2O$ having an interlayer distance of 0.96 nm. The peaks in the 13-40° range of ZrP absorbed ammonia (1.4, 1.8 and 2.0 $mol(NH_3)mol^{-1}(ZrP)$) also includes all the diffraction peaks of $Zr(NH_4PO_4)_2 \cdot H_2O$ (Figure 4.4.1(iii)). It is confirmed

that $Zr(NH_4PO_4)_2 \cdot H_2O$ is present in the ZrP absorbed ammonia. The interplanar spacing calculated by the broad peaks around 2θ of 11.6 ° of ZrP absorbed ammonia (1.4 and 1.8 $mol(NH_3)mol^{-1}(ZrP)$) is similar to the interlayer distance 0.76 nm of ZrP in Figure 4.4.1(i). According to figure 4.3.1 and 4.3.3 of ZrP absorbed ammonia (1.4 and 1.8 $mol(NH_3)mol^{-1}(ZrP)$) and the equation 4.3.2, the broad peak around 2θ of 11.6 ° can be explained by the presence of $Zr(NH_4PO_4)(HPO_4) \cdot H_2O$ having smaller crystallites and defects. A new shoulder at 2θ of 24.5°, not present in ZrP and $Zr(NH_4PO_4)_2 \cdot H_2O$, is shown in the wide angle XRD pattern of ZrP absorbed ammonia (1.4 $mol(NH_3)mol^{-1}(ZrP)$). The new shoulder suggest the presence of $Zr(NH_4PO_4)(HPO_4) \cdot H_2O$. These results can be understood by the coexistence of $Zr(NH_4PO_4)(HPO_4) \cdot H_2O$ and $Zr(NH_4PO_4)_2 \cdot H_2O$ in the range of ammonia storage capacity from 1 to 2 $mol(NH_3)mol^{-1}(ZrP)$. Moreover, the interlayer distance of $Zr(NH_4PO_4)(HPO_4) \cdot H_2O$ is suggested to be about 0.76 nm, similar to that of ZrP.

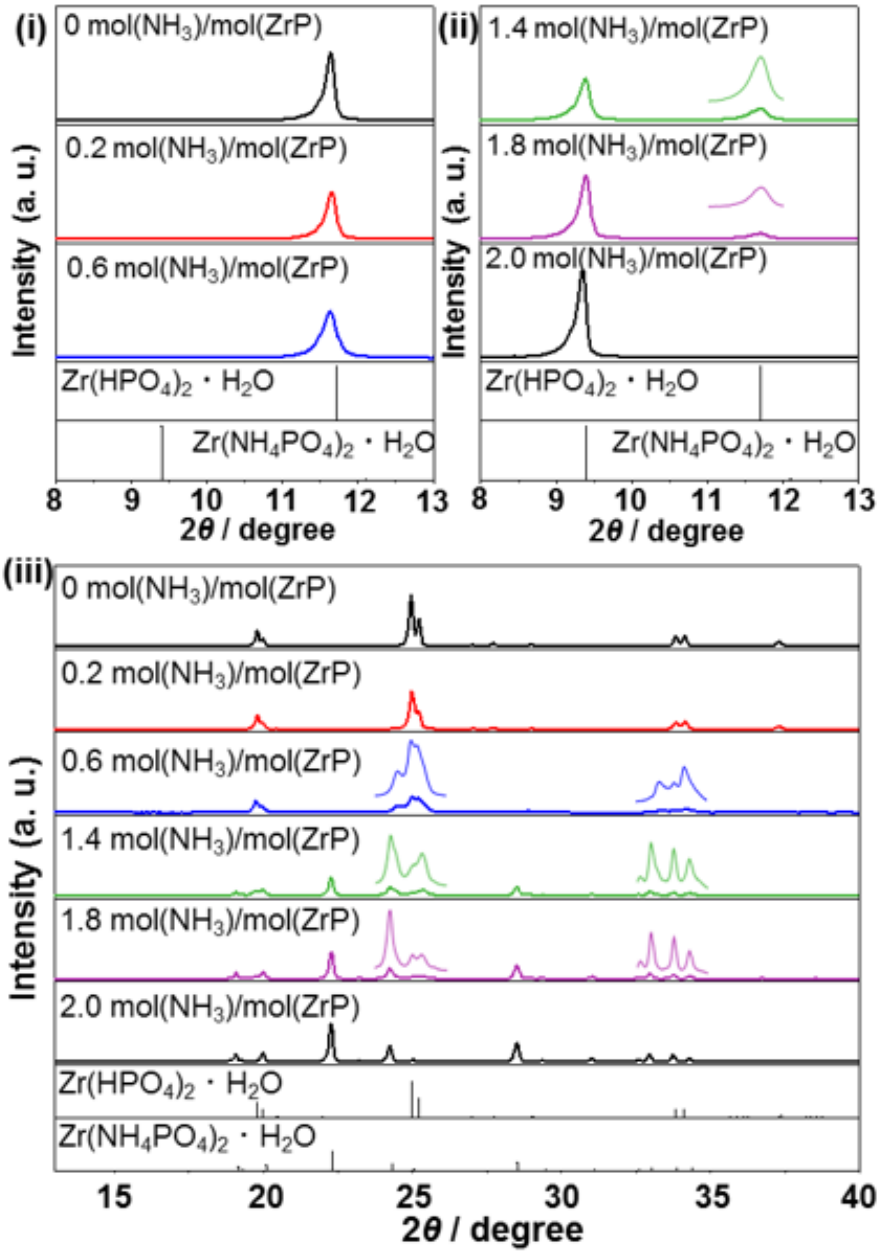

Figure 4.4.1 XRD patterns of ZrP, ZrP absorbed ammonia(ammonia storage capacity: 0.2, 0.6, 1.4, 1.8, and 2.0 mol(NH_3)mol^{-1}(ZrP)), $Zr(HPO_4)_2 \cdot H_2O$ (JCPDS 00-019-1489) and $Zr(NH_4PO_4)_2 \cdot H_2O$ (JCPDS01-071-1633), (i) small angle XRD patterns at 2θ of 8–13° (ammonia storage capacity: 0.2, 0.6 mol(NH_3)mol^{-1}(ZrP)), (ii) small angle XRD patterns at 2θ of 8–13° (ammonia storage capacity: 1.4, 1.8 and 2.0 mol(NH_3)mol^{-1}(ZrP)), (iii) wide angle XRD patterns at 2θ of 13–40° (ammonia storage capacity: 0–2.0 mol(NH_3)mol^{-1}(ZrP)) [20].

4.4.2 Fine structure model of ZrP absorbed ammonia

Figure 4.4.2 shows fine structure models of ZrP and ZrP absorbed ammonia. Zr forms a sheet with a square planar geometry as a unit, and tetrahedral HPO_4^{2-} groups are alternately arranged above and below it to form a layered structure. In the four oxygen atoms bound to the phosphorus atom, the three atoms are bound to Zr and the other one is bound to hydrogen. ZrP and ZrP absorbed ammonia (2.0 mol(NH_3)mol^{-1}(ZrP)) is known to have a layered structure. The interlayer distances are 0.76 nm and 0.96 nm, respectively [22,23]. These results correspond to the peak around 2θ of 11.6 ° and 9.4 ° in the XRD measurement. ZrP absorbed ammonia (1.0 mol(NH_3)mol^{-1}(ZrP)) has also a layered structure such as ZrP.

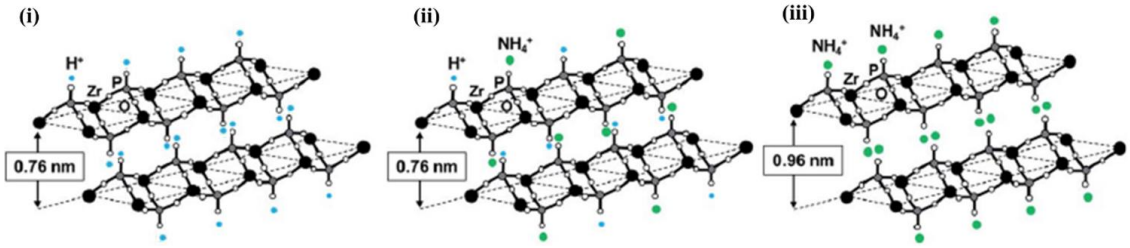

Figure 4.4.2 Fine structural model of ZrP and ZrP absorbed ammonia. (i)ZrP, (ii) ZrP absorbed ammonia (1.0 mol(NH_3)mol^{-1}(ZrP) : ZrP-NH_3) (iii) ZrP absorbed ammonia (2.0 mol(NH_3)mol^{-1}(ZrP) : ZrP-2NH_3)[20].

4.5. Local structure of ZrP absorbed ammonia

4.5.1 ^{31}P MAS NMR spectrum of ZrP absorbed ammonia

The chemical shift reflects the local structure around the 31P nucleus and thus can provide the information on the spatial coordination of ZrP absorbed ammonia. Figure 4.5.1 shows solid ^{31}P MAS NMR spectra of ZrP and ZrP absorbed ammonia (0.4, 1.6 and 2.0 mol(NH_3)mol^{-1}(ZrP)). NMR peaks for ZrP and ZrP absorbed ammonia (2.0 mol(NH_3)mol^{-1}(ZrP): ZrP-2NH_3) were observed at the chemical shift of -18.7 ppm and -16.8 ppm, respectively. These chemical shifts are consistent with the values in the previous paper [24]. The chemical shift of -18.7 ppm indicates ^{31}P in the HPO_4^- group of ZrP [25].

The chemical shift of ZrP-2NH_3 move to the lower magnetic field side compared with that of ZrP. It is presumed that the shielding effect around ^{31}P is changed to smaller by expansion of the interlayer distance of ZrP-2NH_3 (9.6 nm) [24,26], although ZrP and ZrP-NH_3 have same interlayer distance of 7.6 nm.

ZrP absorbed ammonia (0.4 mol(NH_3)mol^{-1}(ZrP)) exhibits a ZrP peak at -18.7 ppm and a new shoulder at -19.3 ppm, respectively. ZrP absorbed ammonia (1.6 mol(NH_3)mol^{-1}(ZrP)) also exhibits a ZrP-2NH_3 peak at -16.8 ppm and a new peak at -19.3 ppm, respectively. It has been reported that X-ray diffractions of ZrP absorbed ammonia (0.4 and 1.6 mol(NH_3)mol^{-1}(ZrP)) indicates the presence of $Zr(NH_4PO_4)(HPO_4)\cdot H_2O$. Thus, it is indicated that the peaks at -19.3 ppm is based on $Zr(NH_4PO_4)(HPO_4)\cdot H_2O$.

The chemical shift of ^{31}P based on $Zr(NH_4PO_4)(HPO_4)\cdot H_2O$ to the higher magnetic field is supposed to be due to a relative increase in the electron density around phosphorus at $Zr(NH_4PO_4)(HPO_4)\cdot H_2O$ compared to that of ZrP. The loan pairs of electrons on ammonia forms a coordinate bond with proton and the electron density of oxygen bonded to the proton in the phosphate group increases. Then, the electron density around ^{31}P at $Zr(NH_4PO_4)(HPO_4)\cdot H_2O$ is expected to increase relative to that of ZrP.

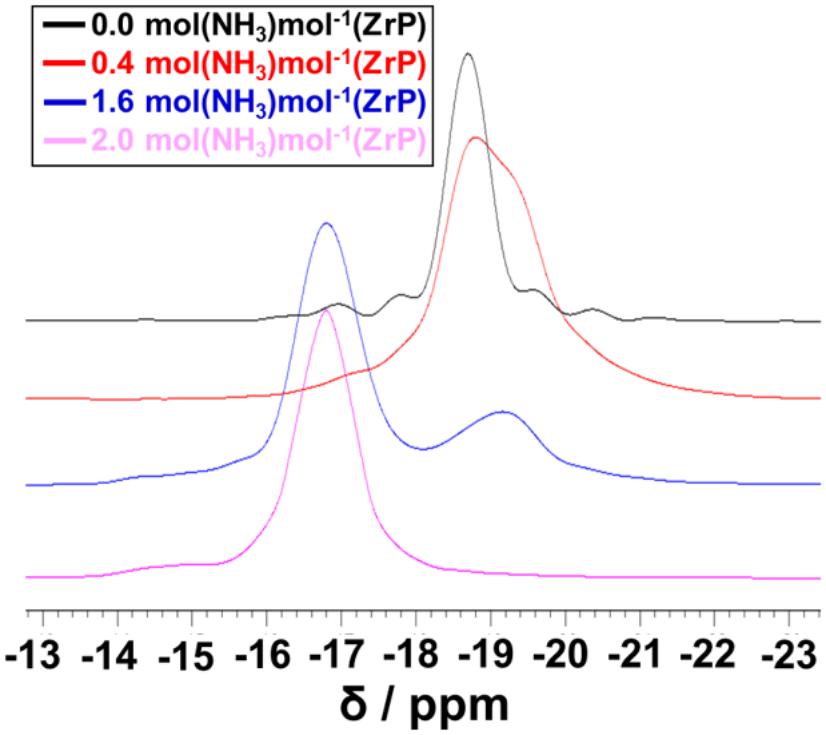

Figure 4.5.1 ^{31}P MAS NMR spectrum of ZrP and ZrP absorbed ammonia (0.4, 1.6 and 2.0 $mol(NH_3)mol^{-1}(ZrP)$)[27].

4.5.2 FTIR spectrum of ZrP absorbed ammonia

Figure 4.5.2 shows FTIR spectra of ZrP and ZrP absorbed ammonia (0.4, 1.6, and 2.0 mol(NH_3)mol^{-1}(ZrP)) in the range from 2000 to 1000 cm^{-1}. Around 1620 cm^{-1}, these peaks indicate the bending vibration of crystalline water (H-O-H). Then, below 1300 cm^{-1}, these peaks are based on the bending variation of H-O-P and the stretching vibration of O-P-O [28,29].

New peaks appear in the range of 1550-1350 cm^{-1} during ammonia absorption. Two peaks are observed at 1440 and 1420 cm^{-1} for ZrP absorbed ammonia (0.4 mol(NH_3)mol^{-1}(ZrP)). The additional peak is observed at 1480 cm^{-1} for ZrP with 1.6 and 2.0 mol(NH_3)mol^{-1}(ZrP). The additional peak correlates with the second plateau concentration of NH_3 in the ZrP absorbed ammonia and the NMR chemical shift of -16.8ppm.

In the range from 1500-1400 cm^{-1}, it has been reported that three FTIR peaks appear for the proton exchanged zeolite absorbed ammonia. It is indicated that these multi peaks are caused by the bending vibration of N-H in NH_4^+ with multiple hydrogen bonds [30]. According to this paper, it is suggested that the reaction of NH_3 with H in Brønsted acid sites of ZrP leads to the formation of NH_4^+ ion in which H has hydrogen bond between O of phosphate groups. Based on the number of FTIR peaks in the range from 1500-1400 cm^{-1}, it is suggested that the ammonium ion in the ZrP with 1.0-2.0 mol(NH_3)mol^{-1}(ZrP) has two hydrogen bonds.

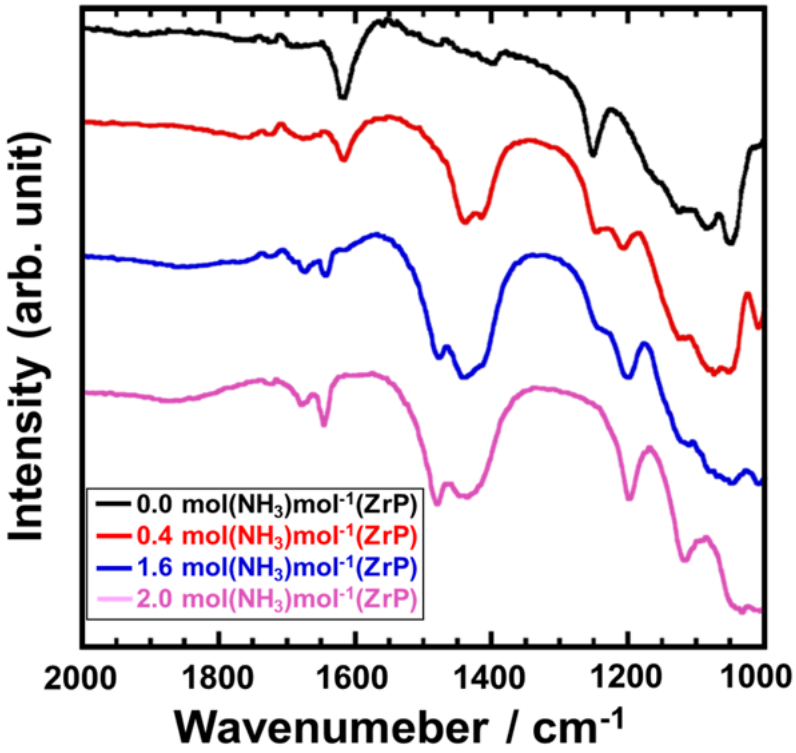

Figure 4.5.2 FTIR spectrum of ZrP and ZrP absorbed ammonia (0.4, 1.6 and 2.0 mol(NH_3)mol^{-1}(ZrP)) in the range between 2000 and 1000 cm^{-1}. The background measurement was performed using a KBr pellet[27].

4.5.3 Local structure model of ZrP absorbed ammonia

Figure 4.5.3(i) shows a local structure model of ZrP. 1 mole of crystalline water exists in the interlayer of 1 mole of ZrP, and 1 mole of ZrP has 2 mole of proton in the phosphate group. Based on ab initio calculation using density functional theory, it is presumed that O in crystalline water and H of phosphate group, and H in crystalline water and O in phosphate group form hydrogen bond. Since all phosphorus is considered to have a similar chemical state, one ^{31}P NMR peak may appear in ZrP.

Figure 4.5.3(ii) shows a local structure model of ZrP-NH_3. 1 mole of ammonia and 1 mole of crystalline water exist in the interlayer of 1 mole of ZrP. FTIR peaks suggest that N in ammonia reacts with H in phosphate group to form N-H coordinate bond in NH_4^+ having hydrogen bonds. The absolute values of ΔH^0 have larger values because of the formation of the coordinate bond (NH_4^+). Thus, ammonia is released at the high temperature of 573 K. Moreover, according to the NMR measurement, the chemical shift of ^{31}P move to the higher magnetic field side compared with ^{31}P of ZrP. It is presumed that the shielding effect around P is larger in the presence of NH_4^+.

Figure 4.5.3(iii) shows a local structure model of ZrP-2NH_3. 2 mole of ammonia and 1 mole of crystalline water exist in the interlayer of 1 mole of ZrP. FTIR peaks suggest that N in ammonia reacts with H in phosphate group to form N-H coordinate bond in NH_4^+ having hydrogen bonds. The number of hydrogen bond between H in NH_4^+ and O in phosphate group of ZrP-2NH_3 is large compared with that of ZrP-NH_3. The larger number of

hydrogen bond of NH_4^+ may reduce the absolute values of ΔH^0. Then, ammonia is released at the lower temperature of 373K.

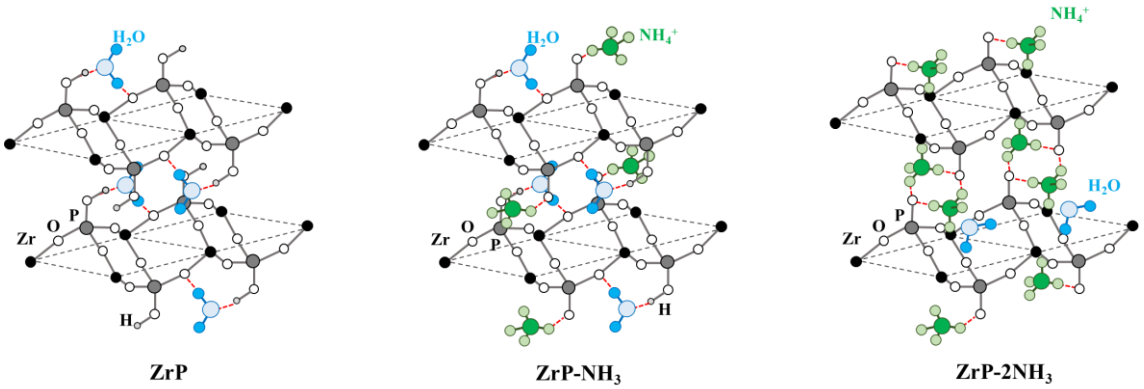

Figure 4.5.3 Local structure model of ZrP absorbed ammonia[27].

4.6 Ammonia removal demonstration test using a new system combined water and ZrP

Figure 4.5 shows the change in ammonia gas concentration over time by addition of water and aqueous dispersion of ZrP. The concentration of ammonia gas decreases with time with the addition of water or the dispersion of ZrP. Compared to water, the dispersion greatly removes the residual ammonia gas concentration in the space, decreasing the ammonia gas concentration to 1 ppm at 120 min and to 0.5 ppm at 240 min. This is because ammonia can be stored in ZrP to low concentrations due to a strong interaction based on the acid-base reaction. Therefore, it is confirmed that the dispersion of ZrP in water is useful as an ammonia removal system to reduce the ammonia gas concentration of leaked ammonia. In addition, since ZrP is insoluble in water, it is possible to separate ZrP absorbed ammonia from water after ammonia removal.

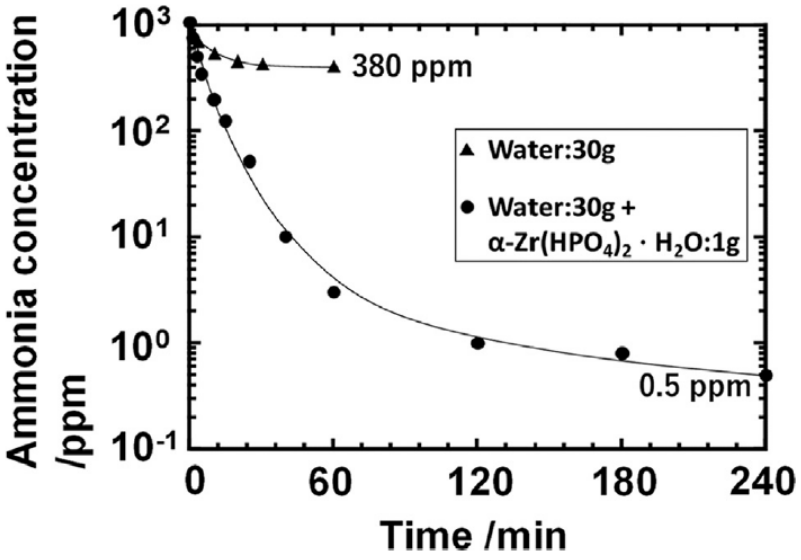

Figure 4.6 Change in ammonia gas concentration over time[20].

References

[1] Y. Kojima, and H. Ikeda, 4-5-3 safety of ammonia as hydrogen and energy carriers. Abstract of papers. 28th annual meeting of the Japan institute of energy tournament; August 7-8, 2019, Osaka.

[2] NIST Chemistry WebBook, Thermophysical Properties of Ammonia, Retrieved December 29th, 2020 from https://webbook.nist.gov/cgi/fluid.cgi?ID=C7664417 &Action=Page

[3] *Chemical Engineering Handbook, rev. 6 Edition*, The Society of Chemical Engineers, Maruzen Co., Ltd., 1999, page 81.

[4] T. Yasuoka, M. Ichinose, A. Saito, J. Takano, and S. Mitsuzawa, *J. Chem. Soc. Jpn. Chem. Ind. Chem.*, **5** (1985) 956-960.

[5] *CRC handbook of chemistry and physics. 97th ed.*, W.M. Haynes, CRC Press, 2016-2017.

[6] S.C. Amendola, S.L. Sharp-Goldman, M.S.Janjua, N.C. Spencer, M.T. Kelly, P.J. Petillo, and M. Binder, *Int. J. Hydrogen Energy*, **25** (2000) 969-975.

[7] Y. Kojima, K. Suzuki, K. Fukumoto, M. Sasaki, T. Yamamoto, Y. Kawai, and H. Hayashi, *Int. J. Hydrogen Energy*, 27 (2002) 1029-1034.

[8] Q. Xu, and M. Chandra, *J. Alloys Compd.*, **446-447** (2007), 729-732.

[9] H. Nishino, *Environ. Technol. Jpn.*, **19** (1990) 643-645.

[10] M. Tsuhako, and H. Nakayama, *J. Soc. Inorg. Mater. Jpn.*, **7** (2000) 679-684.

[11] M. Turco, P. Ciambelli, G. Bagnasco, A. La-Ginestra, P. Galli, and C. Ferragina, *J. Catal.*,117 (1989) 355-361.

[12] M. Kumar, H. Li, X. Zhang, X.C. Zeng, and J.S. Francisco, *J. Am. Chem. Soc.*, **140** (2018) 6456–6466.

[13] K.H. Kim, and O.S. Shin, *ACF. Carbon Sci.*, **2** (2001) 109-112.

[14] M. Dietrch, D. Rauch, U. Simon, A. Porch, and R. Moos, *J. Sensors Sens. Syst.*, **4** (2015) 263-269.

[15] B. Zeynizadeh, S. Rahmani, and S. Ilkhanizadeh, *Polyhedron*, **168** (2019) 48-56.

[16] Y. Kojima, H. Miyaoka, and T. Zhang. *Ammonia detoxification liquid and ammonia detoxification method.* JP2019-89035.

[17] Y. Kojima, and M. Yamaguchi, *Int. J. hydrogen energy*, **45** (2020) 10233-10246.

[18] T. Asada, T. Ohkubo, K. Kawata, and K. Oikawa, J. Health Sci., **52** (2006) 585-589.

[19] M. Yamaguchi, T. Ichikawa, H. Miyaoka, T. Zhang, H. Miyaoka, and Y. Kojima, *Int. J. hydrogen energy*, **45** (2020) 22189-22194.

[20] M. Yamaguchi, H. Miyaoka, and Y. Kojima, *RSC Adv.*, **10** (2020) 20882-20885.

[21] *CRC handbook of chemistry and physics. 97th ed.*, W.M. Haynes, CRC Press, 2016-2017.
[22] L. Sedlakova, and V. Pekarek, *J. Less-Common Met.*, **10** (1966) 130-132.
[23] A. Clearfield, and J. M. Troup, *J. Phys. Chem.*, **77** (1973) 243-247.
[24] D.J. Maclachlan, and K.R. Morgan, *J. Phys. Chem.*, **94** (1990) 7656–7661.
[25] H. Nakayama, T. Eguchi, N. Nakamura, S. Yamaguchi, M. Danjyo, and M. Tsuhako, *J. Mater. Chem.*, **6** (1997) 1063-1066.
[26] D.J. Maclachlan, and K.R. Morgan, *J. Phys. Chem.*, **96** (1992) 3458–3464.
[27] M.Yamaguchi, H. Miyaoka and Y. Kojima, *J. Phys. Chem. C,*, **125**, (2021) 3758-3763.
[28] S.E. Honbsley, D.V. Nowell, D.T. Stewart, *Spectrochim. Acta.*, **30A** (1973) 535-541.
[29] B.N.N. Silva, S.R. Tavares, and A.A. Leitao, *New J. Chem.*, **44** (2020) 10111-10118.
[30] A. Zecchina, L. Marchese, S. Bordiga, C. Paze, and E. Gianotti, *J. Phys. Chem. B*, **101** (1997) 10128-10135.

5. Conclusions

In this study, we focused on insoluble proton based solid acids as materials to be combined with water, and measured the ammonia absorption properties of various insoluble proton based solid acids in ammonia water. Among them, we focused on α-zirconium phosphate (ZrP), which has a layered structure, and analyzed thermodynamic properties and structural changes of ZrP absorbed ammonia.

(i) Ammonia ad/absorption characteristics of insoluble proton-based solid acids

Insoluble proton based solid acids are expected to react with ammonia in water to form insoluble ammonium ion-based materials. We proposed a new ammonia removal system combining water and an insoluble proton-based solid acid.

Then, the ammonia storage capacity and equilibrium concentration of various insoluble proton-based solid acids was measured. Ammonia storage capacity of ZrP from ammonia water showed a maximum value 10.2 wt% among the proton-based solid acids and remove ammonia to low concentrations (1 ppm).

The aqueous dispersion of ZrP can greatly reduce the residual ammonia concentration in the space from 1000 ppm to 0.5 ppm. Since ZrP is insoluble in water after the ammonia absorption, it can be separated easily from water solution.

(ii) Thermodynamic and structural analyses of zirconium phosphate absorbed ammonia.

Thermodynamic analysis

Two ammonia equilibrium plateau concentration was found by ammonia concentration composition isotherm (CCI) measurement. The standard heat of formation ΔH^0 and the standard entropy change ΔS^0 were obtained by van't Hoff plot. As a result, the values of ΔH^0 and ΔS^0 were found to be -95 kJ $mol^{-1}(NH_3)$ and -200 J $K^{-1}mol^{-1}(NH_3)$ for the range of 1-2 $mol(NH_3)mol^{-1}(ZrP)$, respectively. ΔH^0 in the range of 0-1 $mol(NH_3)$ $mol^{-1}(ZrP)$ is considered to be lower than that of 1-2 $mol(NH_3)mol^{-1}(ZrP)$ due to the ammonia equilibrium plateau concentration.

The ammonia desorption temperature of 373 K corresponds to the ammonia absorption of 1-2 $mol(NH_3)mol^{-1}(ZrP)$, and the ammonia desorption temperature of 573 K corresponds to the ammonia absorption of 0-1 $mol(NH_3)mol^{-1}(ZrP)$.

Structural analysis

A two-step structural phase transition was found during ammonia absorption in ZrP. The structural phase transition mainly by the expansion of interlayer distance was confirmed by the X-ray diffraction (XRD). The broad peak around 2θ of 11.6 ° can be explained by the presence of $Zr(NH_4PO_4)(HPO_4)\cdot H_2O$ having smaller crystallites and defects.

The local structures of ZrP absorbed ammonia from 0 to 1

mol(NH_3)mol^{-1}(ZrP) and that from 1 to 2 mol(NH_3)mol^{-1}(ZrP) were different by ^{31}P MAS NMR and FTIR spectroscopy. It was found that ammonia attaches to the phosphate groups of ZrP to form ammonium ion, and ZrP absorbed ammonia (2 mol(NH_3)mol^{-1}(ZrP)) has two hydrogen bonds of one ammonia ion in two places connecting the layers to one phosphate group in each layer.

When ZrP absorbs ammonia in water, the two-step ammonia plateau region, fine structure and local structure changes were observed, which is considered to be a specific result of the layered structure of ZrP. Therefore, a layered structure is the key to a useful ammonia storage material. Also, the specific results obtained by having a layered structure are fascinating from an academic.

Currently, various two-dimensional solid acids have been reported, including layered phosphates with different interlayer distances or different metal atoms. We propose that further analysis of these materials make it possible to synthesize insoluble ammonia storage materials with large ammonia storage capacity and low ammonia equilibrium plateau concentration.

Acknowledgment

I would like to express my sincere appreciation to my supervisor Professor Dr. Yoshitsugu Kojima for his patient guidance, valuable suggestions and useful discussions.

I would also like to express my great appreciation to Professor Dr. Takayuki Ichikawa for his helpful guidance and comments.

Moreover, I would like to express my deepest appreciation to Associate Professor Dr. Hiroki Miyaoka for his thoughtful guidance and discussions.

I gratefully acknowledge Professor Dr. Takashi Suzuki and Professor Dr. Takahiro Onimaru for examining my doctoral thesis.

I am indebt to Mr. Tomoyuki Ichikawa who is Hydrolabo CEO and Mr. Hitoshi Fujitaka who is Hiroshima University's staff for their useful help and discussions.

I am very grateful to all of the laboratory's members, Associate Professor Dr. Ankur Jain, Assistant Professor Dr. Tengfei Zhang, Assistant Professor Dr. Rini Singh, Assistant Professor Dr. Machi Kanna, Dr. Keita Nakajima, Dr. Hiroki Uesato, Dr. Rajesh Kumar, Dr. Fangqin Guo, Dr. Pratibha Pal, Dr. Keita Shinzato, Ms. Hikaru Miyaoka, Mr. Seiki Sugino, Mr. Hiroyuki Gi, Mr. Fernando Cano-Banda, Mr. Pankaj Kumar Singh for their wonderful help and encouragement.

I am also very grateful to the laboratory's staff, Ms. Saori Inagaki, Ms. Misao Mukoda and Mr. Hiroyuki Kurihama for their continuous support and encouragement.

Finally, I would like to thank my family for their understanding and support.